Time-Domain Modeling of Three-Dimensional Earth's and Planetary Electromagnetic Induction Effect in Ground and Satellite Observations

Grayver, Alexander V.; Kuvshinov, Alexey; Werthmüller, Dieter

DOI
10.1029/2020JA028672

Publication date
2021

Document Version
Final published version

Published in
Journal of Geophysical Research: Space Physics

Citation (APA)
Grayver, A. V., Kuvshinov, A., & Werthmüller, D. (2021). Time-Domain Modeling of Three-Dimensional Earth's and Planetary Electromagnetic Induction Effect in Ground and Satellite Observations. *Journal of Geophysical Research: Space Physics*, *126*(3), 1-26. Article e2020JA028672. https://doi.org/10.1029/2020JA028672

JGR Space Physics

RESEARCH ARTICLE
10.1029/2020JA028672

Key Points:

- Accurate modeling of electromagnetic (EM) induction effects in ground and satellite observations via local and global impulse responses
- Including three-dimensional EM induction effects improves description of the observed magnetic variations during both quiet and disturbed conditions
- We provide a data constrained model of external currents for the Swarm era

Correspondence to:
A. V. Grayver,
agrayver@erdw.ethz.ch

Citation:
Grayver, A. V., Kuvshinov, A., & Werthmüller, D. (2021). Time-domain modeling of three-dimensional Earth's and planetary electromagnetic induction effect in ground and satellite observations. *Journal of Geophysical Research: Space Physics*, *126*, e2020JA028672. https://doi.org/10.1029/2020JA028672

Received 29 SEP 2020
Accepted 4 JAN 2021

Time-Domain Modeling of Three-Dimensional Earth's and Planetary Electromagnetic Induction Effect in Ground and Satellite Observations

Alexander V. Grayver[1], Alexey Kuvshinov[1], and Dieter Werthmüller[2]

[1]Institute of Geophysics, ETH Zurich, Zurich, Switzerland, [2]Faculty of Civil Engineering and Geosciences, TU Delft, Netherlands

Abstract Electric currents induced in conductive planetary interiors by time-varying magnetospheric and ionospheric current systems have a significant effect on electromagnetic (EM) field observations. Complete characterization of EM induction effects is difficult owing to nonlinear interactions between the three-dimensional electrical structure of a planet and spatial complexity of inducing current systems. We present, a general framework for time-domain modeling of three-dimensional EM induction effects in heterogeneous conducting planets. Our approach does not assume that the magnetic field is potential, allows for an arbitrary distribution of electrical conductivity within a planet, and can deal with spatially complex time-varying current systems. The method is applicable to both data measured at stationary observation sites and satellite platforms, and enables the calculation of three-dimensional EM induction effects in near real-time settings.

1. Introduction

The effect of electric (telluric) currents induced in subsurface was observed in time series of geomagnetic field variations as early as in Schuster (1889), where it was also proposed that this effect depends on the electrical conductivity at depth. Subsequent studies have led to the establishment of an entirely new research field that exploits the electromagnetic (EM) induction phenomenon to sound planetary interiors (Price, 1967). Nevertheless, present studies focusing on natural current systems, such as in magnetosphere or ionosphere, often neglect the effect of currents induced in the subsurface or treat it by using a variety of simplistic assumptions. However, as model parameterizations have become more realistic and accuracy of the geomagnetic measurements has improved, the effect of induction may no longer be neglected or substantially simplified, creating a need for efficient methods which can accurately account for it.

There exist two principal approaches to account for the induction effects in geomagnetic data. First, one can separate an observed vector magnetic field into inducing (external) and induced (internal) parts by using the classic Gauss method (Gauss, 1877). However, limitations imposed by this method, namely that the magnetic field must be potential and measured in a region between the inducing and induced currents, either restrict or invalidate its applicability. Besides, including more unknowns in statistical models to constrain the induced part may quickly degrade the quality of the models given noisy data with limited coverage. An alternative to that is to model the EM induction effect due to extraneous currents by invoking the governing Maxwell equations.

The latter approach has several advantages. Unlike the Gauss method, the modeling approach is applicable regardless of the position of measurements relative to the inducing and induced current regions, and remains valid in regions where the field is not potential. Additionally, this has a positive effect for the conditioning of statistical models since extra unknowns used to describe the induced part can be eliminated.

In practice, the complication behind modeling EM induction in geomagnetic observations is twofold. First, one needs to assume a subsurface conductivity model. A number of regional and global conductivity models exist. This study will not focus on how these models are constructed and whether they represent the subsurface accurately, even though inaccurate conductivity models may bias results. It is expected that our knowledge about the electrical structure of the subsurface will continuously improve, allowing for the construction of more accurate models at different scales (Kelbert, 2020). Second, even if a distribution of

the subsurface conductivity was known, modeling induced response of a three-dimensional heterogeneous planet remains a computationally demanding problem.

Our goal is to develop an efficient time-domain method for calculating the EM induction effect of a planet with an arbitrary three-dimensional conductivity distribution that is suitable for both ground and satellite observations.

One way to calculate a planet's EM induction effect is through frequency domain (FD) transfer functions, which describe a planet's response due to "elementary" extraneous currents. Modeling three-dimensional EM induction effects with transfer functions was previously applied to analyze daily magnetic field variations (Yamazaki & Maute, 2017) in ground (Guzavina et al., 2019; Koch & Kuvshinov, 2013; Kuvshinov et al., 1999) and satellite measurements (Chulliat et al., 2016; Sabaka et al., 2004, 2015, 2018). Additionally, it was applied in the analysis of aperiodic geomagnetic variations in ground observations (Honkonen et al., 2018; Munch et al., 2020; Olsen & Kuvshinov, 2004; Püthe et al., 2014; Sun et al., 2015). These studies focused on Fourier transformed data and applied transfer functions in FD, followed by inverse Fourier transform in order to obtain results in time domain. Therefore, all aforementioned studies effectively worked in FD.

However, the FD approach based on transfer functions has limitations in many practical scenarios. Among them are applications demanding near real-time predictions of induction effects with constantly augmented time series, such as space weather hazard assessment, or estimation of steering errors in geomagnetic navigation while drilling. The limitations of the FD approach are also apparent when working with data from constantly moving satellites due to spatiotemporal aliasing. To overcome these restrictions, transfer functions can be converted into impulse responses and applied to the data directly in time domain. This approach was adopted by Maus and Weidelt (2004); Olsen et al. (2005); and Thomson and Lesur (2007) for modeling EM induction effects in satellite data. However, these works only considered the induction effect due to an external source described by a single (first zonal) spherical harmonic (SH) function and, moreover, assumed a one-dimensional subsurface conductivity distribution. The extension of this concept to general settings and presentation of all methodological details constitute the main contribution of this study.

Here, we calculate time-domain impulse responses of a medium by converting transfer functions precalculated in FD. We achieve high computational efficiency by applying optimal digital linear filters (DLFs; Ghosh, 1970, 1971a) with the lagged convolution method (Anderson, 1975), which require only a small set of (computationally expensive) FD solutions. For this purpose, we design new DLFs using the methodology presented in Werthmüller et al. (2019). Alternatively, evaluation of impulse responses of a three-dimensional medium can be done by means of dedicated time-domain induction solvers (Velímský et al., 2003; Velímský & Martinec, 2005).

The methods developed here are applied to describe induction effect due to ionospheric and magnetospheric currents in ground and satellite geomagnetic observations. However, the formalism is amenable to observations made around other planets, where conventional methods may be too restrictive (e.g., Olsen et al., 2010).

2. Methods

2.1. Governing Equations

EM field variations are governed by Maxwell's equations. In FD, these equations read

$$\frac{1}{\mu_0}\nabla\times\vec{B} = \sigma\vec{E}+\vec{j}^{\,\mathrm{ext}}, \tag{1}$$

$$\nabla\times\vec{E} = -\mathrm{i}\omega\vec{B}, \tag{2}$$

where μ_0 is the magnetic permeability of free space; ω angular frequency; $\vec{j}^{\,\mathrm{ext}}(\vec{r},\omega)$ the extraneous (impressed) electric current density; $\vec{B}(\vec{r},\omega;\sigma),\vec{E}(\vec{r},\omega;\sigma)$ are magnetic and electric fields, respectively; $\sigma(\vec{r})$ spatial distribution of electrical conductivity; vector $\vec{r}=(r,\vartheta,\varphi)$ describes a position in the spherical coordinate

system with r, ϑ and φ being distance from the planet's center, colatitude, and longitude, respectively. Note that we neglected displacement currents and adopted the following Fourier convention

$$f(t) = \frac{1}{2\pi}\int_{-\infty}^{\infty} \tilde{f}(\omega)e^{i\omega t}\mathrm{d}\omega. \tag{3}$$

We assume that the current density, $\vec{j}^{\,\mathrm{ext}}(\vec{r},\omega)$, can be represented as a linear combination of spatial modes $\vec{j}_i(\vec{r})$,

$$\vec{j}^{\,\mathrm{ext}}(\vec{r},\omega) = \sum_i \vec{j}_i(\vec{r})c_i(\omega), \tag{4}$$

where $\vec{j}_i(\vec{r})$ can, in practice, include electric dipoles, current loops (Sun & Egbert, 2012), or be a continuous function.

By virtue of the linearity of Maxwell's equations with respect to the $\vec{j}^{\,\mathrm{ext}}(\vec{r},\omega)$ term, we can expand total (i.e., inducing plus induced) EM field as a linear combination of individual fields $\vec{B}_i, \vec{E}_i$,

$$\vec{B}(\vec{r},\omega;\sigma) = \sum_i \vec{B}_i(\vec{r},\omega;\sigma)c_i(\omega), \tag{5}$$

$$\vec{E}(\vec{r},\omega;\sigma) = \sum_i \vec{E}_i(\vec{r},\omega;\sigma)c_i(\omega). \tag{6}$$

The $\vec{B}_i(\vec{r},\omega;\sigma)$ and $\vec{E}_i(\vec{r},\omega;\sigma)$ fields are solutions of the equations

$$\frac{1}{\mu_0}\nabla\times\vec{B}_i = \sigma\vec{E}_i + \vec{j}_i, \tag{7}$$

$$\nabla\times\vec{E}_i = -\mathrm{i}\omega\vec{B}_i, \tag{8}$$

and, following definitions in Appendix A, represent EM transfer functions of a medium.

Therefore, a transfer function of a planet at a position $\vec{r}$ depends on the subsurface conductivity distribution and frequency of excitation as well as on the spatial geometry of the current density expressed through the $\vec{j}_i$ term.

2.2. Current Density Representation

We now elaborate on the form of the current density term $\vec{j}^{\,\mathrm{ext}}$. In this study, we assume that electric currents flow within an insulated spherical shell above the ground. This allows us to collapse any current density distribution within the shell into a current sheet characterized by a stream function

$$\vec{j}^{\,\mathrm{ext}}(\vec{r},\omega) = -\delta(r-b)\hat{e}_r\times\nabla_H\Psi(\theta,\phi,\omega), \tag{9}$$

where a is planet's radius, $b = a + h$, with h being the altitude of the current sheet,

$$\nabla_H f = \frac{1}{r}\frac{\partial f}{\partial\theta}\hat{e}_\theta + \frac{1}{r\sin\theta}\frac{\partial f}{\partial\phi}\hat{e}_\phi, \tag{10}$$

and $\hat{e}_r$, $\hat{e}_\theta$ and $\hat{e}_\phi$ are the unit vectors of the spherical coordinate system. Consequently, we can expand the stream function as a linear combination of spatial modes and scalar coefficients, that is

$$\Psi(\theta,\phi,\omega) = \sum_i \Psi_i(\theta,\phi)c_i(\omega). \tag{11}$$

Using Equations 4 and 11, we can rewrite Equation 9 as

$$\vec{j}^{\text{ext}}(\vec{r},\omega) = -\delta(r-b)\sum_i \left[\hat{e}_r \times \nabla_H \Psi_i(\theta,\phi)\right] c_i(\omega). \tag{12}$$

2.3. Spherical Harmonic Representation

The choice of spatial functions Ψ_i is generally problem dependent. In this study, we will adopt SH representation. Then, for an external source, a stream function can be written as (Schmucker, 1985)

$$¤^{e}(\vec{r},\omega) = -\frac{a}{\mu_0}\sum_{(n,m)\in\mathcal{M}} \frac{2n+1}{n+1}\left(\frac{b}{a}\right)^n \tilde{\varepsilon}_n^m(\omega) S_n^m(\theta,\phi), \tag{13}$$

where

$$S_n^m(\theta,\phi) = P_n^{|m|}(\cos\theta)\exp(\mathrm{i}m\phi) \tag{14}$$

is an SH function of degree n and order m with $P_n^{|m|}$ being Schmidt semi-normalized associated Legendre polynomials, and $\mathcal{M}$ is a set of SH functions with corresponding complex-valued SH coefficients $\tilde{\varepsilon}_n^m(\omega)$.

This allows us to rewrite Equation 12 as

$$\vec{j}^{\text{ext}}(\vec{r},\omega) = \sum_{(n,m)\in\mathcal{M}} \vec{j}_n^m(\vec{r})\tilde{\varepsilon}_n^m(\omega), \tag{15}$$

with

$$\vec{j}_n^m(\vec{r}) = \frac{\delta(r-b)}{\mu_0}\frac{2n+1}{n+1}\left(\frac{b}{a}\right)^{n-1} \hat{e}_r \times \nabla_\perp S_n^m(\theta,\phi), \tag{16}$$

where $\nabla_\perp = r\nabla_H$. Accordingly, following Equations 5 and 6, total electric and magnetic fields at a position $\vec{r}$ can be expressed as

$$\vec{B}(\vec{r},\omega;\sigma) = \sum_{(n,m)\in\mathcal{M}} \vec{B}_n^m(\vec{r},\omega;\sigma)\tilde{\varepsilon}_n^m(\omega), \tag{17}$$

$$\vec{E}(\vec{r},\omega;\sigma) = \sum_{(n,m)\in\mathcal{M}} \vec{E}_n^m(\vec{r},\omega;\sigma)\tilde{\varepsilon}_n^m(\omega), \tag{18}$$

where $\vec{B}_n^m, \vec{E}_n^m$ are magnetic and electric field transfer functions due to the current density distribution as given by Equation 16. In what follows, we will work with the magnetic field only, although some applications in the field of space weather modeling may take advantage of Equation 18 to work with electric fields.

Note that Equations 13–18 are only valid for a source that is external relative to the observer. The equivalent derivations for internal sources (such as, for example, ionosphere in satellite data) can be carried out by taking (Schmucker, 1985)

$$\Psi^i(\vec{r},\omega) = \frac{a}{\mu_0}\sum_{(n,m)\in\mathcal{M}} \frac{2n+1}{n}\left(\frac{a}{b}\right)^{n+1} \tilde{\imath}_n^m(\omega) S_n^m(\theta,\phi) \tag{19}$$

instead of Equation 13.

2.4. Impulse Responses and Transfer Functions

In this section, we present methods to calculate EM signals induced by an electric current of the form 16 and measured on the ground or in space.

2.4.1. Local Impulse Responses

For reasons that we discussed in the introduction, it is often more convenient to work with data in time domain. Therefore, total magnetic field at a location $\vec{r}$ and time t can be best described by Equation 17 after its transformation to time domain. Equation 17 can be written in time domain as a convolution integral (see Appendix A for more details)

$$\vec{B}(\vec{r},t;\sigma) = \sum_{(n,m)\in\mathcal{M}^+} \int_{-\infty}^{t} \left[\vec{B}_n^{m(c)}(\vec{r},t-\tau;\sigma) q_n^m(t) + \vec{B}_n^{m(s)}(\vec{r},t-\tau;\sigma) s_n^m(t) \right] \mathrm{d}\tau, \tag{20}$$

where $\mathcal{M}^+$ is a set of SH functions with nonnegative orders ($m \geq 0$); q, s inducing SH coefficients; $\vec{B}_n^{m(c)}$ and $\vec{B}_n^{m(s)}$ are impulse responses of a medium for the q_n^m and s_n^m coefficients, respectively. They can be defined as

$$\vec{B}_n^{m(c)}(\vec{r},t;\sigma) = -\frac{2}{\pi} \int_0^{\infty} \mathrm{Im}\left[\frac{\vec{B}_n^m(\vec{r},\omega;\sigma) + \vec{B}_n^{-m}(\vec{r},\omega;\sigma)}{2} \right] \sin(\omega t) \mathrm{d}\omega \tag{21}$$

and

$$\vec{B}_n^{m(s)}(\vec{r},t;\sigma) = \frac{2}{\pi} \int_0^{\infty} \mathrm{Im}\left[\frac{\vec{B}_n^m(\vec{r},\omega;\sigma) - \vec{B}_n^{-m}(\vec{r},\omega;\sigma)}{2\mathrm{i}} \right] \sin(\omega t) \mathrm{d}\omega. \tag{22}$$

The integrals in Equations 21 and 22 are evaluated by using the DLF method as explained in Appendix B.

2.4.2. Global Impulse Responses

For satellite measurements, using local impulse responses becomes impractical since they require calculating Equations 21 and 22 for every satellite location. Therefore, to describe EM induction effects in satellite data, we resort to different transfer functions, namely, Q-responses and Q-matrices, which enable factorization of spatial and temporal effects. We note, however, that while transfer functions in Equation 17 are valid everywhere, Q-responses and Q-matrices are valid only in regions where the magnetic field is potential.

Recall that if a magnetic field at a position $\vec{r}$ and time t is potential, we have

$$\vec{B}(\vec{r},t;\sigma) = -\nabla\left[V^e(\vec{r},t) + V^i(\vec{r},t;\sigma) \right], \tag{23}$$

where inducing and induced parts of the potential are given by

$$\begin{aligned} V^e(\vec{r},t) &= a \sum_{n=1}^{N} \sum_{m=0}^{n} \left[q_n^m(t)\cos(m\phi) + s_n^m(t)\sin(m\phi) \right] \left(\frac{r}{a} \right)^n P_n^m(\cos\theta) \\ &= \mathrm{Re}\left\{ a \sum_{n=1}^{N} \sum_{m=-n}^{m} \varepsilon_n^m(t) \left(\frac{r}{a} \right)^n S_n^m(\theta,\phi) \right\} \end{aligned} \tag{24}$$

and

$$\begin{aligned} V^i(\vec{r},t;\sigma) &= a \sum_{k=1}^{K} \sum_{l=0}^{k} \left[g_k^l(t;\sigma)\cos(l\phi) + h_k^l(t;\sigma)\sin(l\phi) \right] \left(\frac{a}{r} \right)^{k+1} P_k^l(\cos\theta) \\ &= \mathrm{Re}\left\{ a \sum_{k=1}^{K} \sum_{l=-k}^{k} t_k^l(t;\sigma) \left(\frac{a}{r} \right)^{k+1} S_k^l(\theta,\phi) \right\}, \end{aligned} \tag{25}$$

where N, K are some constants that truncate series. Note that we stated the magnetic field potential using both real-valued and complex-valued notations with the following relation between the coefficients,

$$\varepsilon_n^m = \begin{cases} \dfrac{q_n^m - \mathrm{i}s_n^m}{2}, & m > 0 \\ \dfrac{q_n^{|m|} + \mathrm{i}s_n^{|m|}}{2}, & m < 0. \\ q_n^m, & m = 0 \end{cases} \tag{26}$$

The relation between induced (internal in our case) coefficients g_k^l, h_k^l and ι_k^l is derived in an identical way.

We can now rewrite the induced magnetic field 25 using transfer functions instead of induced SH coefficients. Before presenting the general case, we first consider a case when a planet's conductivity distribution is assumed to be one-dimensional, that is, $\sigma(\vec{r}) \equiv \sigma(r)$. In this case, each coefficient ε_n^m induces one internal coefficient of the same degree and order (e.g., Price, 1967). Inducing and induced coefficients can be related via a scalar transfer function called Q_n-response. In FD, this relation reads

$$\iota_n^m(\omega;\sigma) = Q_n(\omega;\sigma)\varepsilon_n^m(\omega). \tag{27}$$

Note that Q_n is independent of order m (Schmucker, 1985).

Following derivations in Appendix A, transforming Equation 27 to time domain and separating spatial sine and cosine terms leads to a pair of convolution integrals

$$g_n^m(t;\sigma) = Q_n * q_n^m = \int_{-\infty}^{t} Q_n(t-\tau;\sigma) q_n^m(\tau)\mathrm{d}\tau, \tag{28}$$

$$h_n^m(t;\sigma) = Q_n * s_n^m = \int_{-\infty}^{t} Q_n(t-\tau;\sigma) s_n^m(\tau)\mathrm{d}\tau. \tag{29}$$

Subsequently, substituting Equations 28 and 29 in Equation 25 yields internal magnetic potential

$$V^i(\vec{r},t;\sigma) = V^{i(c)}(\vec{r},t;\sigma) + V^{i(s)}(\vec{r},t;\sigma) \tag{30}$$

with

$$V^{i(c)}(\vec{r},t;\sigma) = a \sum_{(n,m)\in\mathcal{M}^+} \left[Q_n * q_n^m\right] \cos(m\phi) \left(\frac{a}{r}\right)^{n+1} P_n^m(\cos\theta), \tag{31}$$

$$V^{i(s)}(\vec{r},t;\sigma) = a \sum_{(n,m)\in\mathcal{M}^+} \left[Q_n * s_n^m\right] \sin(m\phi) \left(\frac{a}{r}\right)^{n+1} P_n^m(\cos\theta). \tag{32}$$

Note that in a one-dimensional case, inducing and induced expansions are identical, hence we used n, m in Equations 27–32 for all SH coefficients.

For a general three-dimensional conductivity distribution, $\sigma(\vec{r})$, in a planet, each coefficient ε_n^m induces infinitely many internal coefficients (Olsen, 1999). The relation between inducing and induced coefficients is then described by a set of transfer functions called Q-matrix

$$\tilde{\iota}_k^l(\omega;\sigma) = \sum_{n,m} \tilde{Q}_{kn}^{lm}(\omega;\sigma)\tilde{\varepsilon}_n^m(\omega). \tag{33}$$

An element of the Q-matrix is given by (Püthe & Kuvshinov, 2014)

$$\tilde{Q}_{kn}^{lm}(\omega;\sigma) = \frac{1}{(k+1)\,\|\,S_k^l\,\|^2} \oiint_{\mathcal{S}(1)} \left[B_{n,r}^m(\vec{r}_a,\omega;\sigma) - B_{n,r}^{m,\mathrm{ext}}(\vec{r}_a)\right] S_k^{l*}(\theta,\phi)\sin\theta\,\mathrm{d}\theta\mathrm{d}\phi, \tag{34}$$

where * denotes complex conjugation, $\vec{r}_a = (a,\theta,\phi)$ is the position vector at the surface of a planet, and $\mathcal{S}(1)$ the surface of a ball with unit radius. The radial magnetic field $B^m_{n,r}$ is (numerically) computed for a given three-dimensional Earth's model induced by a unit amplitude ($\tilde{\varepsilon}^m_n = 1$) SH current source described by Equation 16, and

$$B^{m,\mathrm{ext}}_{n,r}(\vec{r}_a) = -nS^m_n(\theta,\phi) \tag{35}$$

is the inducing (external) part of the radial magnetic field.

In this case, the internal magnetic potential becomes

$$V^{i(c)}(\vec{r},t;\sigma) = a \sum_{(n,m)\in\mathcal{M}^+} \sum_{k,l} \left[Q^{lm,qg}_{kn} * q^m_n + Q^{lm,sg}_{kn} * s^m_n \right] \cos(k\phi) \left(\frac{a}{r}\right)^{k+1} P^l_k(\cos\theta), \tag{36}$$

$$V^{i(s)}(\vec{r},t;\sigma) = a \sum_{(n,m)\in\mathcal{M}^+} \sum_{k,l} \left[Q^{lm,qh}_{kn} * q^m_n + Q^{lm,sh}_{kn} * s^m_n \right] \sin(k\phi) \left(\frac{a}{r}\right)^{k+1} P^l_k(\cos\theta), \tag{37}$$

where

$$\sum_{k,l} = \sum_{k=1}^{K} \sum_{l=0}^{k}. \tag{38}$$

After some algebra, impulse responses in Equations 36 and 37 can be calculated via sine transform (see Equation A9) of the spectra, which are related to the FD Q-matrix (Equation 33) via equations below (the dependence on ω and σ is omitted).

For $l > 0$, $m > 0$:

$$\tilde{Q}^{lm,qg}_{kn} = \frac{\tilde{Q}^{lm}_{kn} + \tilde{Q}^{l-m}_{kn} + \tilde{Q}^{-lm}_{kn} + \tilde{Q}^{-l-m}_{kn}}{2}, \tag{39}$$

$$\tilde{Q}^{lm,qh}_{kn} = \mathrm{i}\frac{\tilde{Q}^{lm}_{kn} + \tilde{Q}^{l-m}_{kn} - \tilde{Q}^{-lm}_{kn} - \tilde{Q}^{-l-m}_{kn}}{2}, \tag{40}$$

$$\tilde{Q}^{lm,sg}_{kn} = \mathrm{i}\frac{-\tilde{Q}^{lm}_{kn} + \tilde{Q}^{l-m}_{kn} - \tilde{Q}^{-lm}_{kn} + \tilde{Q}^{-l-m}_{kn}}{2}, \tag{41}$$

$$\tilde{Q}^{lm,sh}_{kn} = \frac{\tilde{Q}^{lm}_{kn} - \tilde{Q}^{l-m}_{kn} - \tilde{Q}^{-lm}_{kn} + \tilde{Q}^{-l-m}_{kn}}{2}, \tag{42}$$

for $l = 0$, $m > 0$:

$$\tilde{Q}^{0m,qg}_{kn} = \frac{\tilde{Q}^{0m}_{kn} + \tilde{Q}^{0-m}_{kn}}{2}, \tag{43}$$

$$\tilde{Q}^{0m,sg}_{kn} = \mathrm{i}\frac{-\tilde{Q}^{0m}_{kn} + \tilde{Q}^{0-m}_{kn}}{2}, \tag{44}$$

for $l > 0$, $m = 0$:

$$\tilde{Q}^{l0,qg}_{kn} = \tilde{Q}^{l0}_{kn} + \tilde{Q}^{-l0}_{kn}, \tag{45}$$

$$\tilde{Q}^{l0,qh}_{kn} = \mathrm{i}(\tilde{Q}^{l0}_{kn} - \tilde{Q}^{-l0}_{kn}), \tag{46}$$

and for $l = 0$, $m = 0$:

$$\tilde{Q}_{kn}^{00,qg} = \tilde{Q}_{kn}^{00}. \tag{47}$$

Note that both internal potentials, Equations 31 and 32 and Equations 36 and 37, depend only on the pre-calculated Q and inducing coefficients. Additionally, Q does not depend on location, making it particularly well suited for satellite data.

2.5. Determination of Inducing Coefficients

The methods presented in the previous sections enable estimation of timeseries of inducing coefficients in discrete non-overlapping time intervals (time windows). Let us define time intervals of length Δt. We assume that inducing coefficients are piece-wise constant within these time intervals. Then, convolution integrals such as Equation 20 or Equations 28 and 29 can be approximated by discrete sums. For instance, for a time window centered at t we can rewrite Equation 28 as

$$g_n^m(t;\sigma) \approx \sum_{j=0}^{N_t} I_{Q_n}(j;\sigma) q_n^m(t - j\Delta t), \tag{48}$$

where

$$I_{Q_n}(j;\sigma) = \int_{j\Delta t - \Delta t/2}^{j\Delta t + \Delta t/2} Q_n(t;\sigma)\mathrm{d}t. \tag{49}$$

Similar expressions are obtained for other convolution integrals.

With this, coefficients for a time window centered at t can be estimated by solving a minimization problem,

$$\mathbf{q}^*, \mathbf{s}^* = \arg\min_{\mathbf{q},\mathbf{s}} \sum_{i\in\mathcal{D}_t} \sum_{\alpha\in\{\theta,\phi\}} \left[B_{\alpha,i}^o - \sum_{(n,m)\in\mathcal{M}^+} B_{n,\alpha}^m(\vec{r}_i,t;\sigma) \right]^2, \tag{50}$$

where $\mathcal{D}_t$ is a set of magnetic field observations in the current time window with $B_{\alpha,i}^o$ being the measured horizontal magnetic field component at location $\vec{r}_i$ and time t_i; $\mathbf{q},\mathbf{s} \in \mathcal{M}^+$ are vectors of inducing SH coefficients for the given time window; and the modeled fields are given by

$$B_{n,\alpha}^m(\vec{r}_i,t;\sigma) = \sum_{j=0}^{N_t} \left[I_{n,\alpha}^{m(c)}(\vec{r}_i,j;\sigma) q_n^m(t - j\Delta t) + I_{n,\alpha}^{m(s)}(\vec{r}_i,j;\sigma) s_n^m(t - j\Delta t) \right]. \tag{51}$$

For ground observations (see Section 2.4.1), we used

$$I_{n,\alpha}^{m(c)}(\vec{r}_i,j;\sigma) = \int_{t_j - \Delta t/2}^{t_j + \Delta t/2} B_{n,\alpha}^{m(c)}(\vec{r}_i,\tau;\sigma)\mathrm{d}\tau, \tag{52}$$

$$I_{n,\alpha}^{m(s)}(\vec{r}_i,j;\sigma) = \int_{t_j - \Delta t/2}^{t_j + \Delta t/2} B_{n,\alpha}^{m(s)}(\vec{r}_i,\tau;\sigma)\mathrm{d}\tau. \tag{53}$$

Note that the two equations above are valid for magnetic fields computed both for one-dimensional and three-dimensional conductivity models.

For satellite measurements (see Section 2.4.2) and a one-dimensional subsurface conductivity distribution, we take

$$I_{n,\theta}^{m(c)}(\vec{r}_i,j;\sigma) = -I_{Q_n}(j;\sigma) \left(\frac{a}{r_i}\right)^{n+2} \left.\frac{\mathrm{d}P_n^m(\cos\theta)}{\mathrm{d}\theta}\right|_{\theta=\theta_i} \cos(m\phi_i), \tag{54}$$

$$I^{m(c)}_{n,\phi}(\vec{r}_i, j;\sigma) = I_{Q_n}(j;\sigma)\left(\frac{a}{r_i}\right)^{n+2} \frac{m}{\sin\theta_i} P^m_n(\cos\theta_i)\sin(m\phi_i), \tag{55}$$

$$I^{m(s)}_{n,\theta}(\vec{r}_i, j;\sigma) = -I_{Q_n}(j;\sigma)\left(\frac{a}{r_i}\right)^{n+2} \left.\frac{\mathrm{d}P^m_n(\cos\theta)}{\mathrm{d}\theta}\right|_{\theta=\theta_i} \sin(m\phi_i), \tag{56}$$

$$I^{m(s)}_{n,\phi}(\vec{r}_i, j;\sigma) = -I_{Q_n}(j;\sigma)\left(\frac{a}{r_i}\right)^{n+2} \frac{m}{\sin\theta_i} P^m_n(\cos\theta_i)\cos(m\phi_i). \tag{57}$$

Similar, although more lengthy, expressions can be derived using Equations 36 and 37 for a three-dimensional subsurface conductivity distribution.

Note that since we have eliminated internal coefficients, it suffices to use only horizontal magnetic field components in Equation 50 to determine inducing coefficients. This allows for more accurate description of the inducing source since horizontal components are less sensitive to the currents induced in the subsurface compared to the vertical component (Kuvshinov, 2008). Since the problem is linear with respect to inducing coefficients, we used a Huber-weighted robust regression method to find the minimizer of 50.

For every time window, the performance of the model can be evaluated by means of a R^2 statistics, called coefficient of determination. To define it, let us assume that for a given field component all observations and modeled fields in a time window j are collected into vectors $\mathbf{b}^{\mathrm{obs}}_j$ and $\mathbf{b}^{\mathrm{mod}}_j$ such that

$$\mathbf{r}_j = \mathbf{b}^{\mathrm{obs}}_j - \mathbf{b}^{\mathrm{mod}}_j \tag{58}$$

is the vector of residuals. Then

$$R^2_j = 1 - \frac{\langle \mathbf{r}_j, \mathbf{r}_j \rangle}{\langle \mathbf{b}^{\mathrm{obs}}_j - \bar{b}^{\mathrm{obs}}_j, \mathbf{b}^{\mathrm{obs}}_j - \bar{b}^{\mathrm{obs}}_j \rangle} \tag{59}$$

is the coefficient of determination for time window j. Here $\bar{b}^{\mathrm{obs}}_j$ denotes the mean value of $\mathbf{b}^{\mathrm{obs}}_j$ and $\langle \cdot, \cdot \rangle$ is an inner product. Note that we assumed a uniform measurement error of 1 nT when calculating R^2.

2.6. Determination of Induced Coefficients

Previous sections concentrated on evaluation of inducing coefficients. Once they are estimated, we can evaluate induced coefficients that describe EM fields induced in the planetary interior. This is useful in induction studies, where pairs of inducing and induced coefficients are used to estimate subsurface transfer functions, which can be ultimately inverted for the electrical conductivity distribution in the subsurface (Püthe & Kuvshinov, 2014).

By adopting our approach, induced coefficients can be estimated from the radial component alone. This is advantageous since the radial field exhibits higher sensitivity to the subsurface induction effects and was excluded from the estimation of the inducing coefficients (see Equation 50).

Provided that the inducing coefficients q^m_n, s^m_n were estimated following the approach presented in the previous section, the induced part of the total magnetic field can be isolated. In particular, for the observed radial magnetic field,

$$B^{\mathrm{int,o}}_r(\vec{r},t) = B^{\mathrm{o}}_r(\vec{r},t) - B^{\mathrm{ext,o}}_r(\vec{r},t), \tag{60}$$

where

$$B^{\mathrm{ext,o}}_r(\vec{r},t) = -\sum_{(n,m)\in\mathcal{M}^+} \left[q^m_n(t)\cos(m\phi) + s^m_n(t)\sin(m\phi) \right] n\left(\frac{r}{a}\right)^{n-1} P^m_n(\cos\theta), \tag{61}$$

is the inducing part of the radial field (see Equation 23).

Following Equation 25, the remaining induced part of the radial field above the ground can be expanded as

$$B_r^{\text{int}}(\vec{r},t) = \sum_{k,l}\Big[g_k^l(t)\cos(k\phi) + h_k^l(t)\sin(k\phi)\Big](k+1)\left(\frac{a}{r}\right)^{k+2} P_k^l(\cos\theta), \tag{62}$$

which is suitable for the estimation of the induced coefficients in a statistical manner. Specifically, we can estimate coefficients for a time bin centered at $t = j\Delta t$ by solving a minimization problem

$$\mathbf{g}^*,\mathbf{h}^* = \arg\min_{\mathbf{g},\mathbf{h}} \sum_{i\in\mathcal{D}_t}\left[B_{r,i}^{\text{int,o}} - \sum_{k,l}\Big[g_{k,j}^l\cos(k\phi_i) + h_{k,j}^l\sin(k\phi_i)\Big](k+1)\left(\frac{a}{r_i}\right)^{k+2} P_k^l(\cos\theta_i)\right]^2. \tag{63}$$

Therefore, by virtue of Equations 50 and 63 pairs of inducing $\mathbf{q}^*$, $\mathbf{s}^*$ and induced $\mathbf{g}^*$, $\mathbf{h}^*$ coefficients can be estimated in time bins of constant length Δt, providing input data for mantle conductivity studies. Note that estimation of inducing and induced coefficients can be performed repeatedly with updated mantle conductivity models.

3. Data

3.1. Geomagnetic Observatories

We applied the developed methods to ground geomagnetic observatory data. Specifically, we took a set of quality-controlled measurements of the hourly mean vector magnetic field compiled by the British Geological Survey (Macmillan & Olsen, 2013). We concentrate here on the *Swarm* era measurements by using data collected between December 01, 2013 and November 01, 2019. The model of the core and crustal fields as given by the Comprehensive Inversion (CI) model (Sabaka et al., 2018) was subtracted. The distribution of the observatories over the time range used in this study is shown in Figure 1. We further excluded observatories poleward of the 56° and equatorward of 5° geomagnetic latitudes. Thus, the variations in the remaining data set are predominantly driven by the midlatitude ionospheric and magnetospheric currents. The polar and equatorial latitudes are excluded because the present distribution of geomagnetic observatories cannot adequately resolve spatiotemporal structures of the dominant current systems at these latitudes.

3.2. Geomagnetic Satellites

We used nearly 6 years (December 01, 2013 to November 01, 2019) of the geomagnetic field measurements taken by the *Swarm* Alpha and Bravo satellites. Similar to the observatory data, core and crustal fields as given by the CI model were subtracted. The time windows of 3 hours were used, which corresponds to two full orbits and aims to improve the data coverage within a window. Here, we concentrate on studying the EM induction effects of the large-scale magnetosphere currents of external origin and thus the dayside data, namely, between 5 a.m. and 7 p.m. local time, were excluded.

4. Results

4.1. Transfer Functions and Impulse Responses

All transfer functions and corresponding impulse responses referred to as "one-dimensional" were calculated by taking a conductivity model that consists of the one-dimensional conductivity profile from Grayver et al. (2017) with a 7,000 S conductance layer that represents average conductance of the oceans and sediments. For the results referred to as "three-dimensional", a laterally heterogeneous conductivity shell of 1/4° resolution was used to account for the variations in the ocean bathymetry and thickness of sediments. For the one-dimensional case, transfer function were calculated analytically,

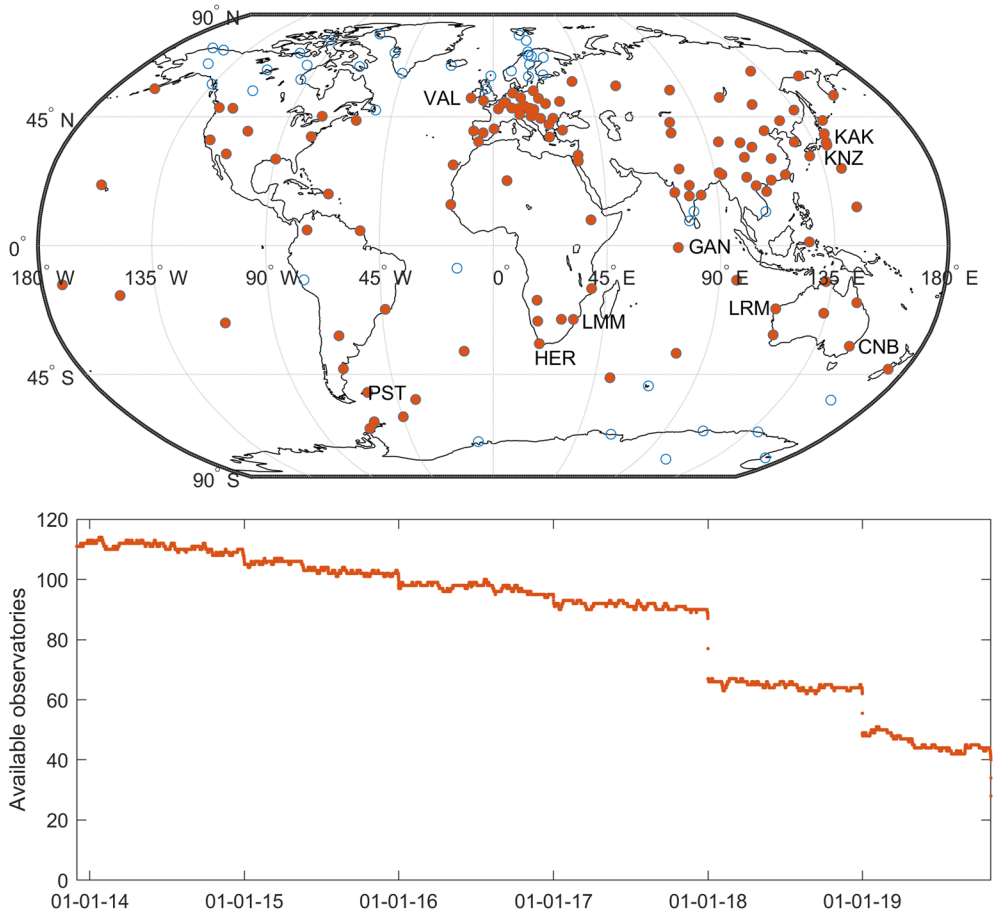

Figure 1. Top: Distribution of geomagnetic observatories. Location of geomagnetic observatories are denoted with circles. Filled circles show observatories used in this study, after discarding locations at high and equatorial geomagnetic dipole latitudes. Bottom: number of used observatories over the time period of the study.

whereas three-dimensional transfer functions were calculated numerically by solving Maxwell's equations in a spherical shell with a Finite Element code GoFEM (Arndt et al., 2020; Grayver et al., 2019; Grayver & Kolev, 2015).

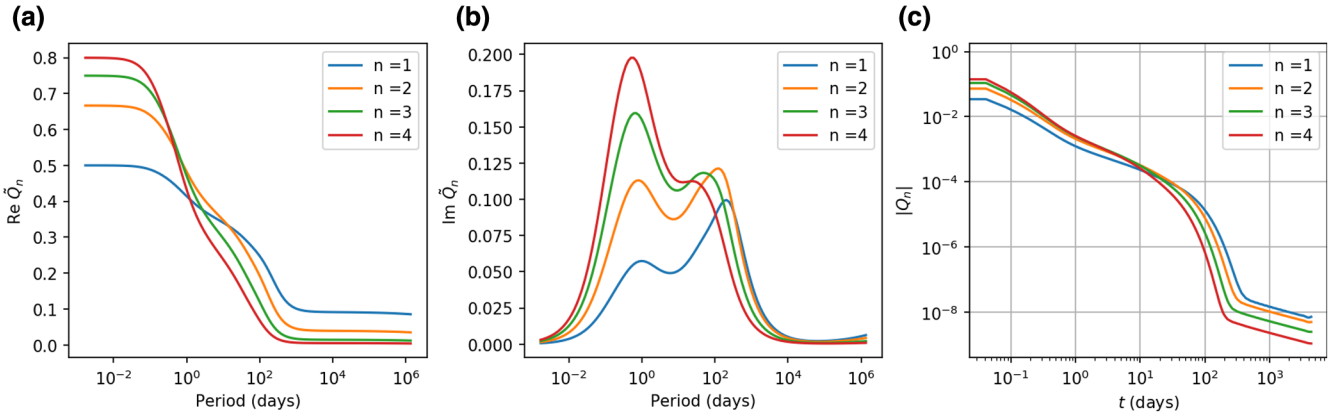

Figure 2. Real (a) and imaginary (b) parts of the $\tilde{Q}_n$ transfer functions (Equation 27) for different degrees n and one-dimensional conductivity profile of Grayver et al. (2017). The magnitudes of the corresponding discrete impulse responses (Equation 49) are shown in plot (c).

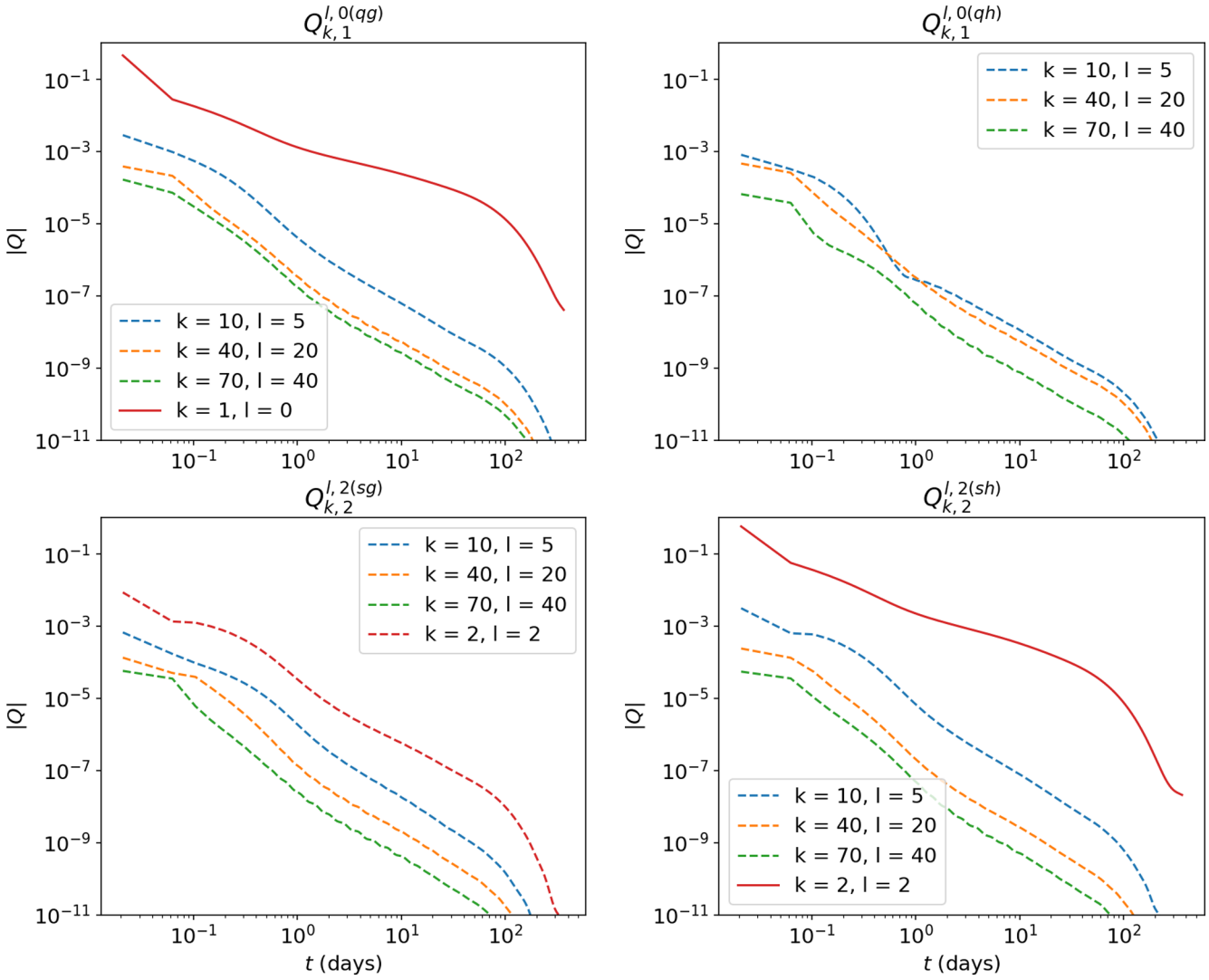

Figure 3. A selection of the three-dimensional discrete impulse responses from the $Q^{lm,qg}_{kn}$ and $Q^{lm,qh}_{kn}$ matrices (Equations 36 and 37) due to the q^0_1 (top row) and s^2_2 (bottom row) inducing terms. Dashed lines denote responses which are nonzero only in the case of a three-dimensional conductivity distribution.

Figure 2 shows one-dimensional transfer functions and corresponding discrete impulse responses. As expected, we see that the decay rate for responses with higher degrees n is faster, implying that attenuation rate of the induced currents increases with the SH degrees of the inducing field. At periods of 1 year and longer, real part of the transfer function flattens as a result of the transient induction effect of the core, which has a finite conductivity (Velímský et al., 2003).

Figure 3 shows a selection of discrete impulse responses from the three-dimensional Q-matrix for different external and internal degrees and orders. First of all, note that in three-dimensional, the matrix is dense, that is, each inducing coefficient leads to infinitely many induced coefficients. However, we observe that the diagonal elements dominate the matrix, whereas off-diagonal entries are generally smaller and decay with the SH degree.

Finally, Figure 4 shows examples for local impulse responses at several observatory locations where both one-dimensional and three-dimensional responses are plotted to highlight the effect of the ocean and sed-

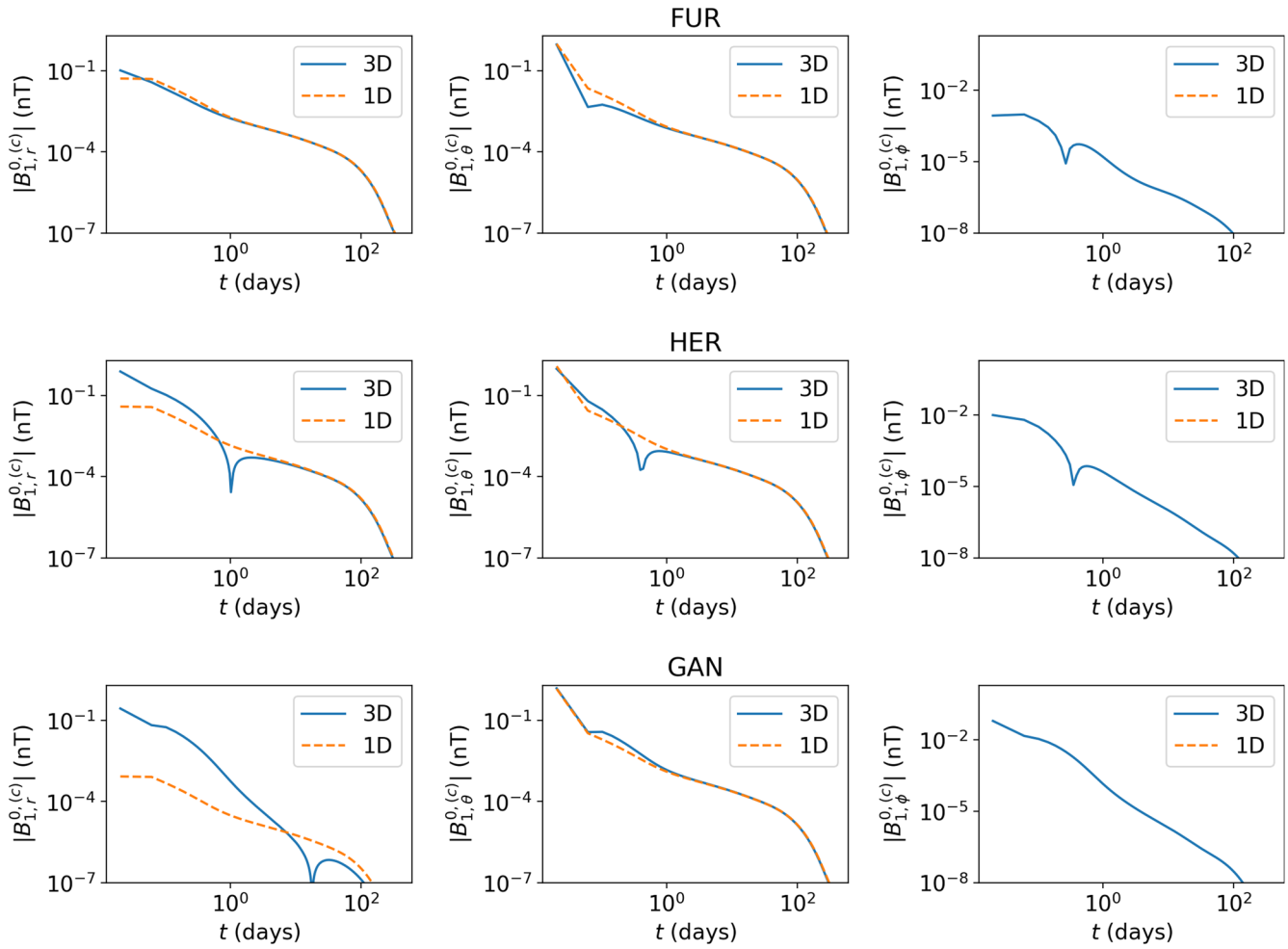

Figure 4. Magnetic field discrete impulse responses (Equation 21) due to a q_1^0 inducing field for three magnetic field components (columns) at three locations: Fürstenfeldbruck (FUR), Hermanus (HER) and Gan, Maldives (GAN). Both one-dimensional (dashed lines) and three-dimensional responses (solid lines) are shown.

imentary cover on impulse responses. We see that the difference between one-dimensional and three-dimensional responses is particularly large for island and coastal locations.

4.2. Model of External Magnetic Field Variations from Ground Observations

We determined SH coefficients up to degree $n_{\max} = 3$ and order $m_{\max} = 3$ within hourly time bins. The length of impulse responses was set to six months, thus transient effects older than 6 months are neglected. This choice is justified since impulse responses for time lags larger than 6 months are $\leq 10^{-6}$ (see Figures 2–4), thus the transient effects become negligible for the majority of practical applications. Other details pertained to data preprocessing and the method of evaluating SH coefficients are given in Sections 3.1 and 2.5, respectively.

The coefficients were determined using both one-dimensional and three-dimensional impulse responses from horizontal magnetic field components (B_θ, B_ϕ). Subsequently, coefficient of determination R^2 was calculated for every time bin using Equation 59 and three components separately, including B_r component, which was not used for the model construction. Figure 5 shows histograms of R^2 coefficient for one-dimensional and three-dimensional models. One apparent observation is a significantly better fit of the radial component with a three-dimensional conductivity model. The fit for horizontal components is virtually

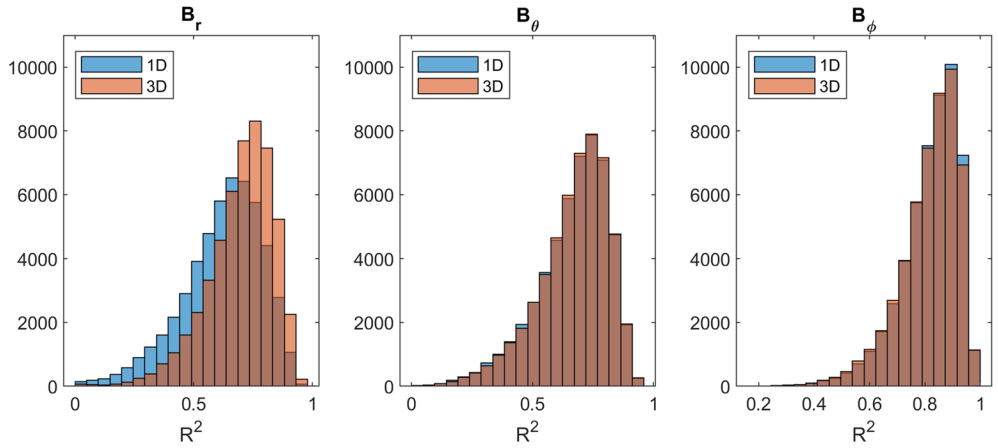

Figure 5. Histograms of the R^2 statistics (coefficient of determination) for individual magnetic field components (from left to right: B_r, B_θ, B_ϕ) and all time windows. The R^2 statistics was determined following Equation 59 between observatory hourly means data and model predictions. The model details are described in Section 4.2.

identical, and the differences are minute and likely fall within the modeling and observation errors. Noteworthy that among all components, the highest coherency is observed for the longitudinal component. These observations confirm that our model, especially the one based on a three-dimensional conductivity model, has a predictive power.

To test how the model performs during different magnetic conditions, we further plot histograms of R^2 statistics for times when magnetic variations are dominated by magnetospheric disturbances (here defined as $|Dst| > 40$ nT) in Figure 6. Although we still observe a significant improvement in coherency for B_r, generally the correlation is lower for B_r, B_θ, whereas it remains high for the longitudinal component. Further, we plot R^2 histograms for times when $Kp \leq 2$ in Figure 7. The reason to use Kp instead of Dst this time is to emphasize the quiet ionosphere conditions. Similar to the examples with disturbed magnetosphere, we again observe significant improvements in the radial component for the three-dimensional model. In comparison with the previous case, however, we see systematically higher R^2 values for all components. Therefore, our model exhibits a better fit during quiet times. Further, the improved fit of the B_r enabled by the three-dimensional model is observed for all times and magnetic conditions, indicating that proper inclusion of the ocean effect is essential when modeling both magnetospheric and ionospheric variations.

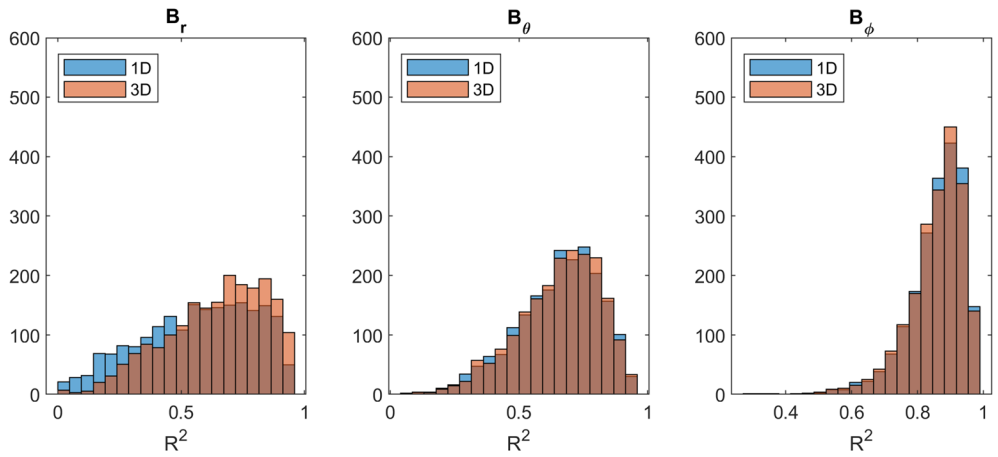

Figure 6. Same as Figure 5, but restricted to time windows when $|Dst| > 40$ nT.

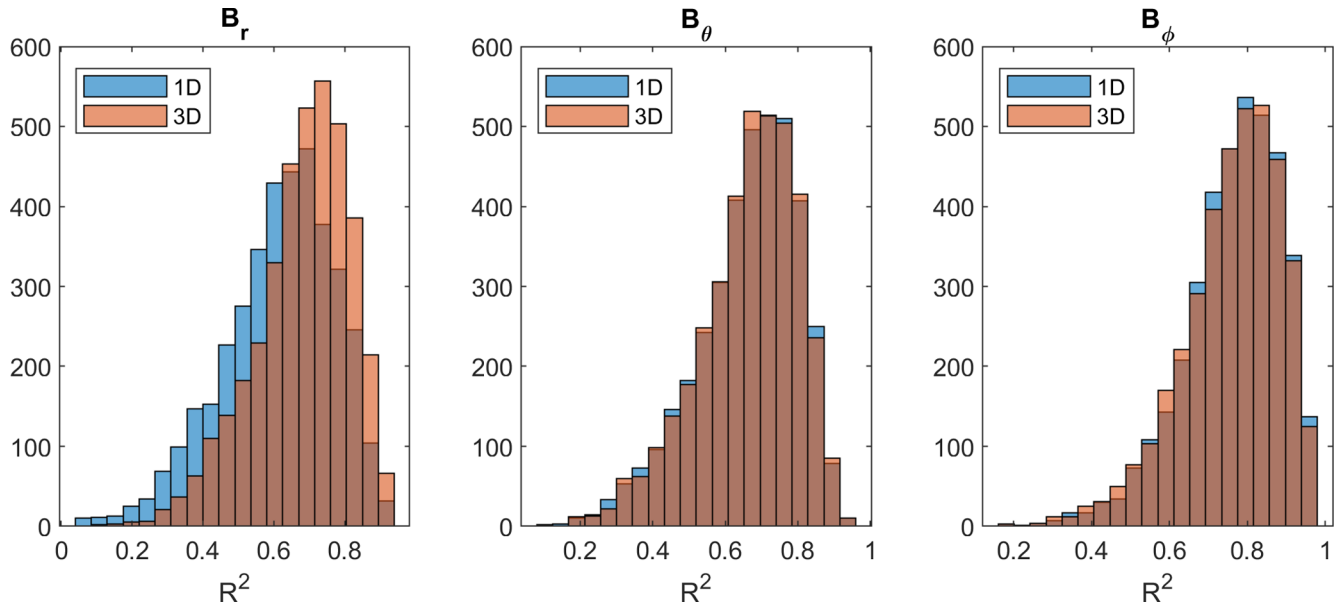

Figure 7. Same as Figure 5, but restricted to time windows when $Kp \leq 2$.

To better quantify the effect of the improved fit due to the usage of a three-dimensional model, we calculated the ratio of three-dimensional and one-dimensional R^2 values for radial magnetic field component at all observatory locations. These values, plotted as a function of the distance to the shoreline, are shown in Figure 8. We observe the improved fit at virtually all locations with the most significant improvement up to a factor of 11 for observations that are ≤200 km from the coast. However, even locations as far as 3,000 km exhibit considerably better fit. This is explained by including the conductance of continental sediments in our three-dimensional model.

Finally, we inspect the observed and modeled time series at a selection of coastal and island observatories. Here, we also added predictions based on the Dst index, calculated as

$$B_r^{\mathrm{Dst}}(\vec{r},t) = \Big[\mathrm{Est}(t) - 2\mathrm{Ist}(t)\Big]\cos\theta \tag{64}$$

$$B_\theta^{\mathrm{Dst}}(\vec{r},t) = -\Big[\mathrm{Est}(t) + \mathrm{Ist}(t)\Big]\sin\theta \tag{65}$$

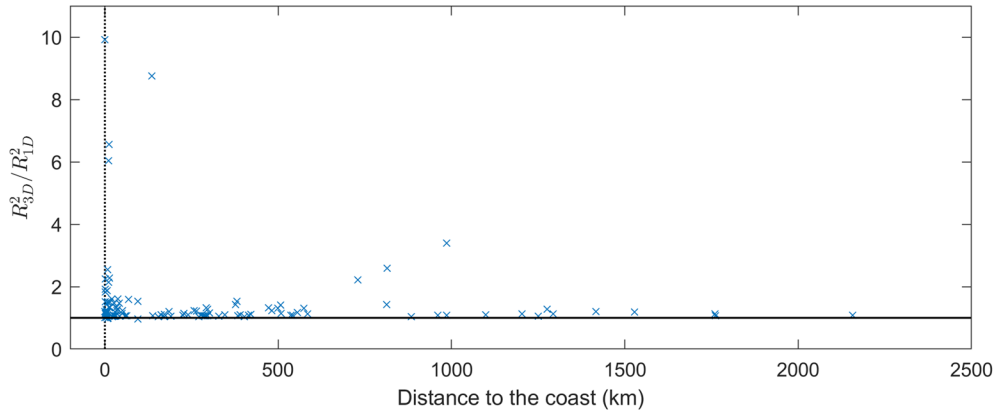

Figure 8. Ratio of the three-dimensional to one-dimensional models R^2 coefficients for B_r field at individual observatories plotted versus distance to the shoreline. Values larger than one indicate improvement over the one-dimensional model.

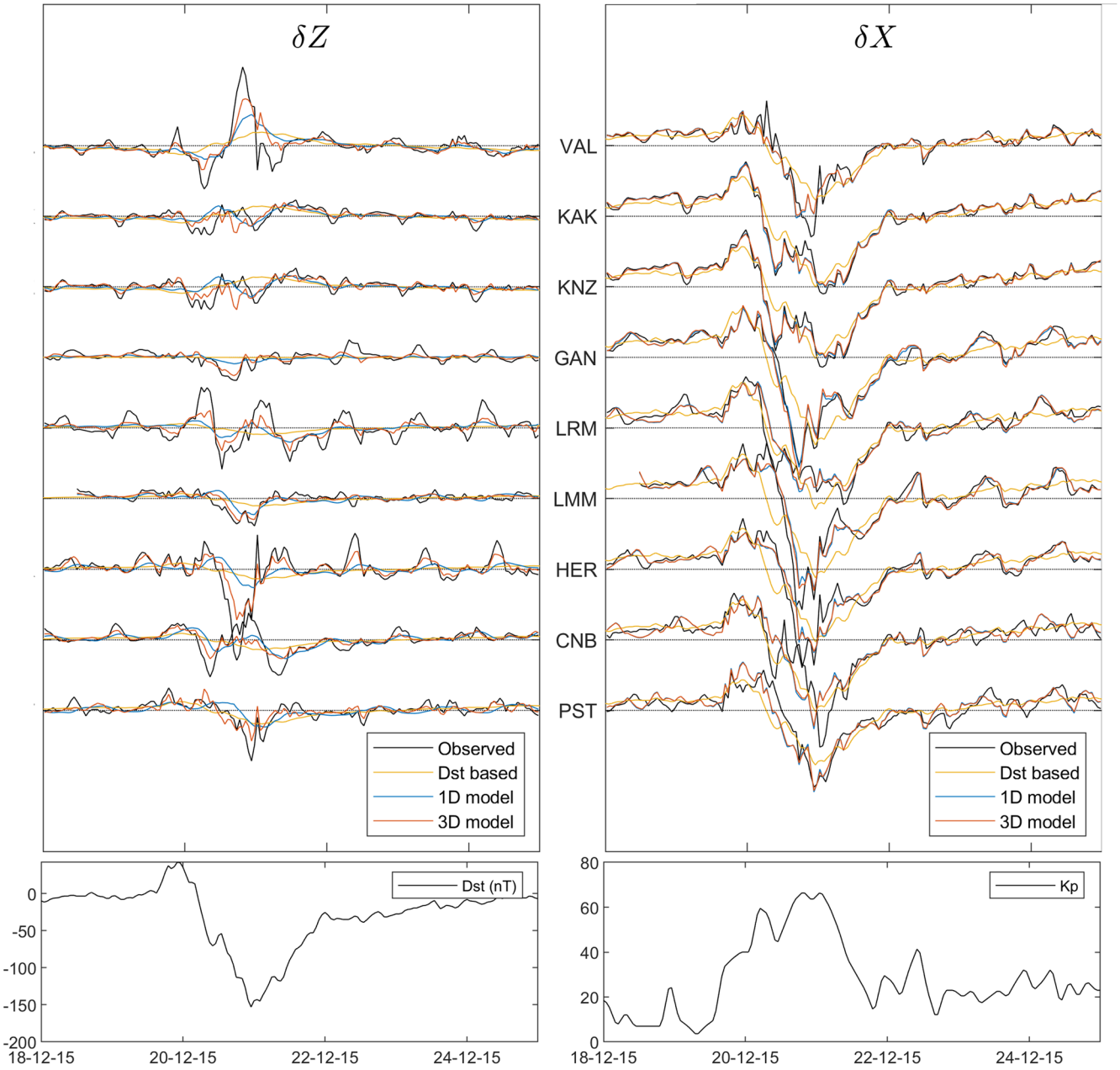

Figure 9. Time series of observed and modeled variations in horizontal ($\delta X = -\delta B_\theta$) and radial ($\delta Z = -\delta B_r$) components at a set of observatories, ordered by latitude. Predictions based on one-dimensional and three-dimensional conductivity models are shown along with D_{st}-based fields (Equation 64). The offset between dotted lines is 100 nT. Lower panels show corresponding D_{st} and Kp indices. See Figure 1 for locations of selected observatories.

$$B_\phi^{\mathrm{Dst}}(\vec{r},t) = 0, \tag{66}$$

where $\mathrm{Dst}(t) = \mathrm{Est}(t) + \mathrm{Ist}(t)$ is a sum of inducing and induced terms (Maus & Weidelt, 2004; Olsen et al., 2005). Figures 9 and 10 each show one week of observed magnetic field variations and model predictions. These periods were chosen since they cover both magnetically disturbed and quiet conditions.

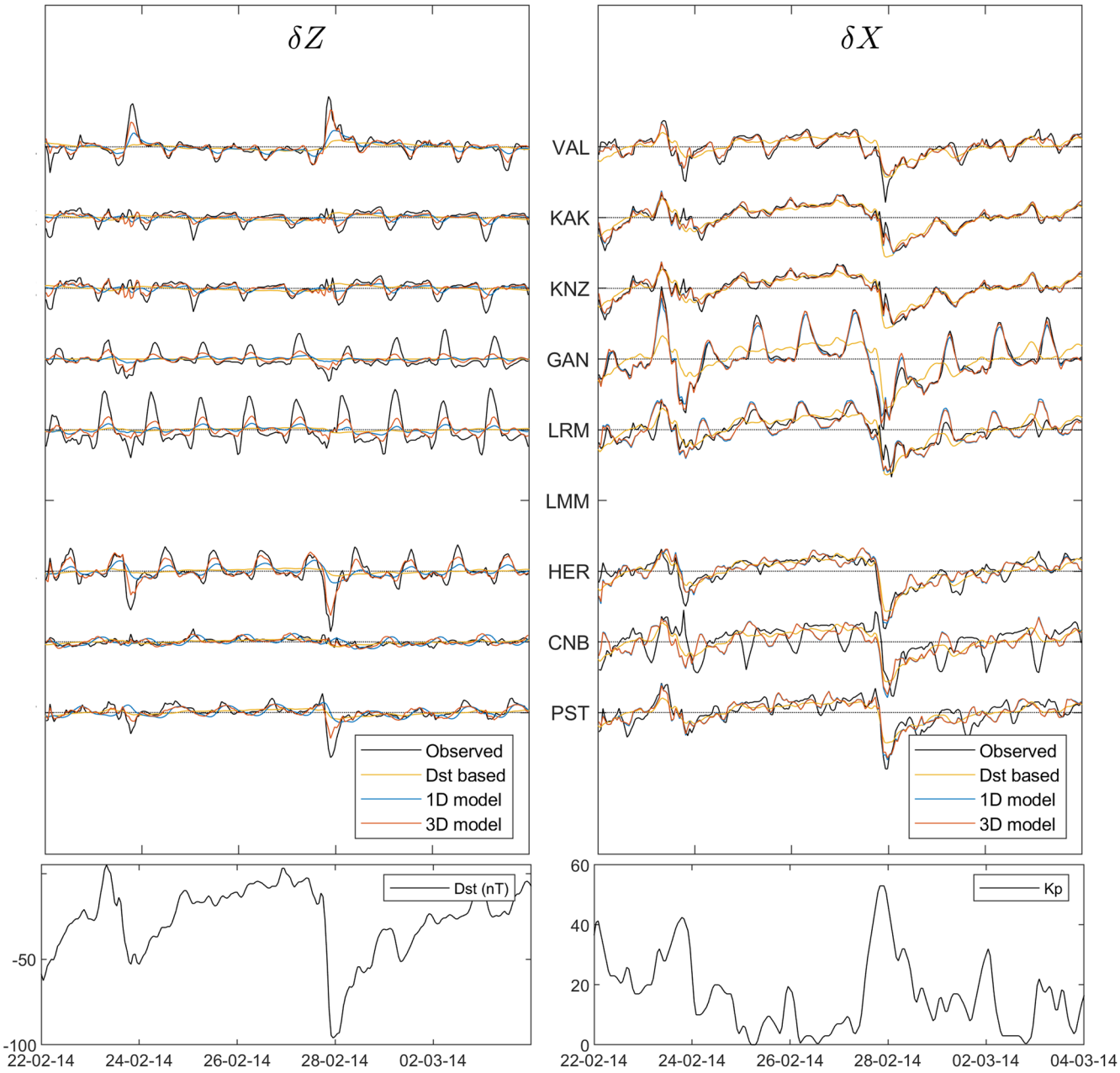

Figure 10. Same as Figure 9, but for a different time period.

The origin of the discrepancy in amplitude between the observed and modeled fields is twofold: (i) we used the global average mantle conductivity profile whereas in reality the bulk subsurface conductivity varies laterally; and (ii) slightly larger discrepancy for quiet times indicates that the adopted SH parameterization with $n_{\max} = 3$, $m_{\max} = 3$ is still insufficient to explain these variations, mostly related to ionospheric currents (Guzavina et al., 2019; Schmucker, 1999).

Additionally, Figures 11 and 12 show spatial distribution of the magnetic field as predicted by estimated external coefficients and a three-dimensional conductivity model. Much stronger influence of three-dimensional EM induction effects in the B_r components is clearly visible. Most of these effects occur near coastal areas and strong lateral conductivity gradients.

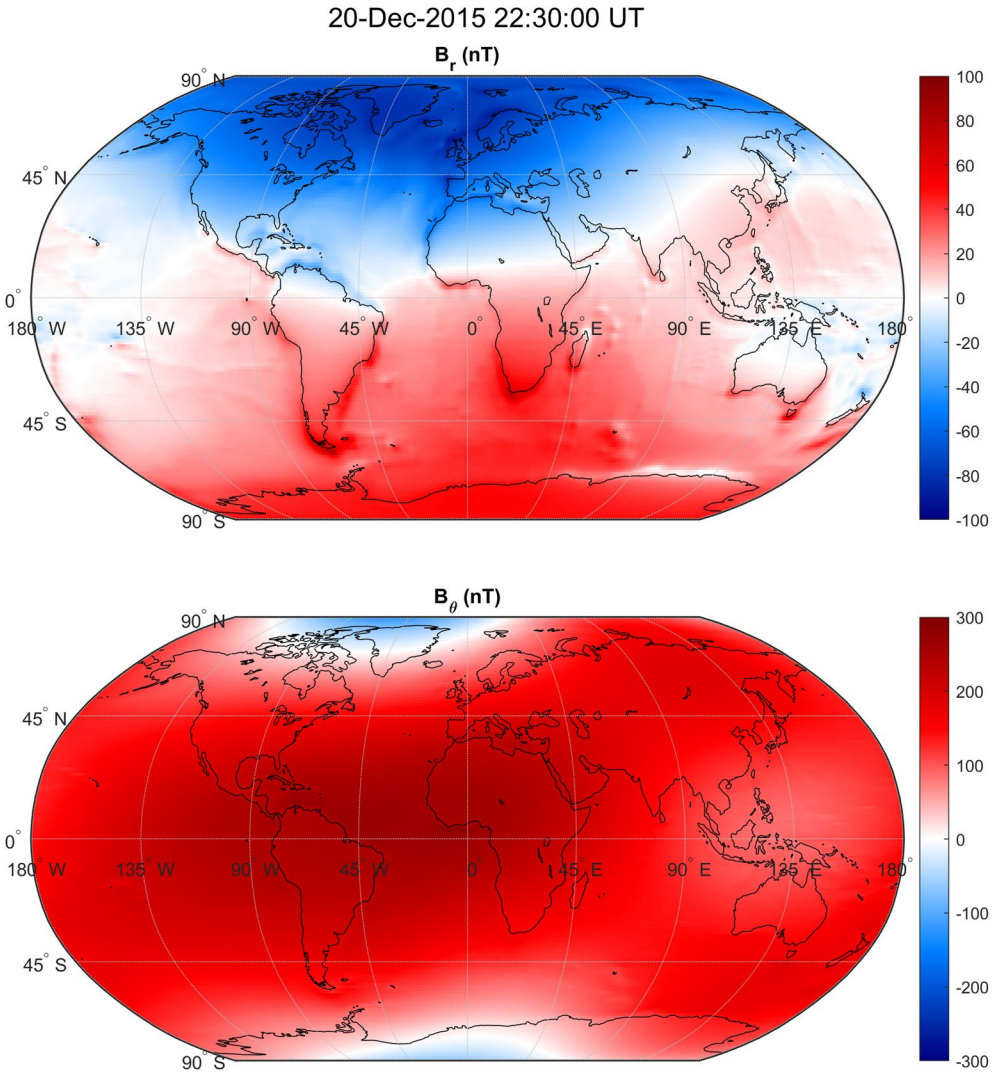

Figure 11. Maps of the radial (top) and horizontal (bottom) components of modeled magnetic field variations at a surface. Predictions based on the three-dimensional conductivity model for a given UT instance are shown. The recorded D_{st} index value at this instance was −155 nT. Significant coastal electromagnetic induction effects are visible in the radial component.

4.3. Model of Magnetospheric Ring Current Variations from *Swarm* Observations

In this section, the model of inducing coefficients was determined by using only satellite data, which was described in Section 3.2. Since we work with nightside data and two satellites, we determined SH coefficients up to degree $n_{\max} = 2$ and order $m_{\max} = 1$ using time bins of 3 h. Therefore, the resolution of this model is much lower than the model in previous section that was based on observatory data. Other parameters pertained to data preprocessing and evaluation of SH coefficients are described in Sections 3.2 and 2.5, respectively.

As in the previous section, we first look at the distribution of R^2 statistics for all time bins and magnetic field components (see Figure 13). First observation that we make is that R^2 values are very similar between one-dimensional and three-dimensional models, indicating that the three-dimensional induction effect from the ocean is largely attenuated at satellite altitudes. Interestingly that now we also have much higher R^2 values for the radial component compared to the B_θ, even though B_r was not used in the construction of the model. One possible explanation are signals that mostly affect horizontal (B_θ, B_ϕ) components at midlatitudes, such as those generated by F-region ionospheric currents (Olsen, 1997). These signals cannot be explained by our low-resolution parameterization that is based on the potential field assumption. To test this

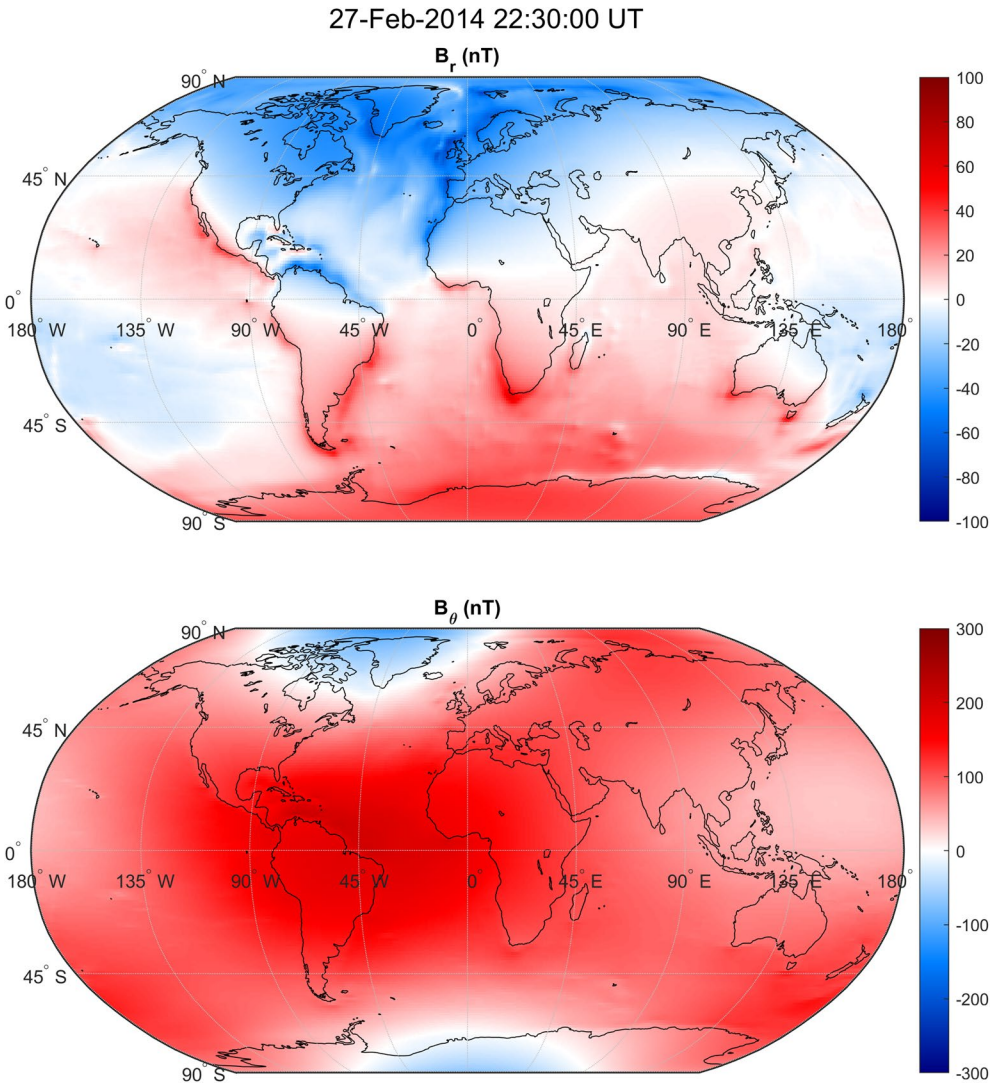

Figure 12. Same as Figure 11, but for a different time. The D_{st} index value at this instance was −95 nT.

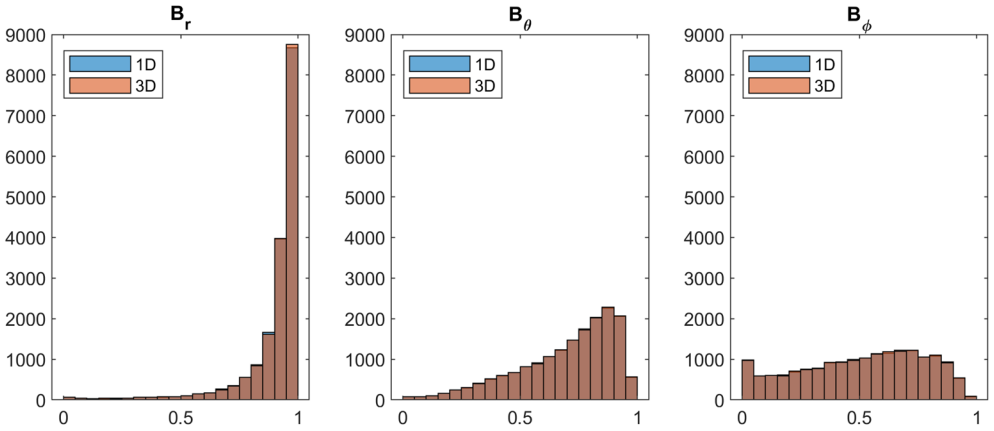

Figure 13. Histograms of the R^2 statistics (coefficient of determination) for individual magnetic field components and all time windows. The R^2 statistics was determined following Equation 59 between observatory data and predictions from satellite data model described in Section 4.3.

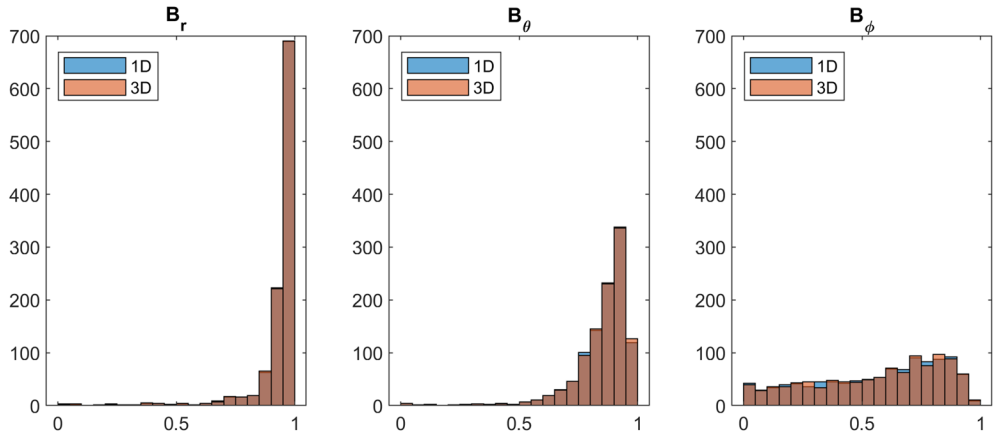

Figure 14. Same as Figure 13, but restricted to time windows when $Kp \leq 2$.

hypothesis, histograms limited to the time windows for which $Kp \leq 2$ are shown in Figure 14. Indeed, during periods with the less disturbed ionosphere we obtain significantly higher values of R^2 for the B_θ component.

Finally, Figure 15 plots time series of the q_1^0 coefficient determined using the observatory and satellite data. For reference, we also plot the D_{st} index. We observe very good match between coefficients estimated from satellite and observatory data, confirming the validity of both models and approaches.

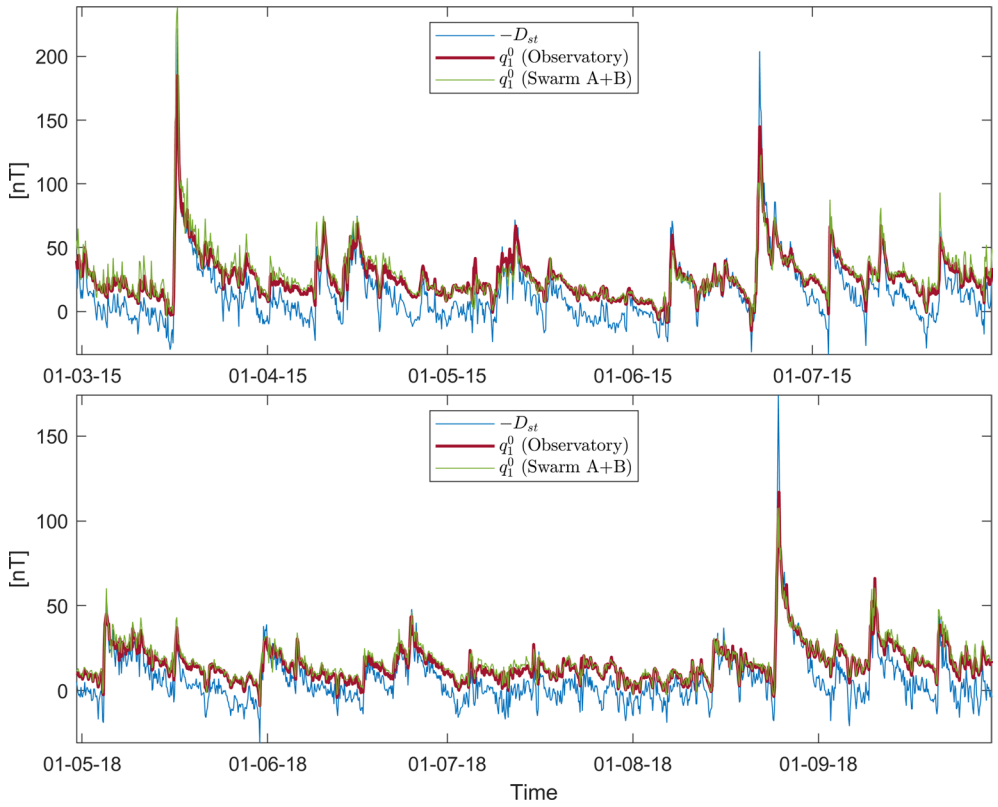

Figure 15. Time series of the first zonal spherical harmonic coefficient, q_1^0, as given by satellite (Section 4.3) and observatory (Section 4.2) data based models in geomagnetic coordinate frame. Two five-month intervals featuring quiet and disturbed magnetic conditions are shown. For comparison, the negative D_{st} magnetic index is plotted. Systematic offset in D_{st} against q_1^0 seen in Figure 15 is due to the absence of stable quiet time ring current in the D_{st} index.

5. Conclusions

The EM induction effect from a time-varying magnetic field significantly influences magnetic field observations, where it can be both a polluting signal to be removed or a primary signal to study (e.g., mantle induction and space weather applications). We showed that the inducing currents of ionospheric and magnetospheric origin can be effectively estimated while the effect of the planetary induced response is modeled. This work has presented a unified framework for modeling EM induction effects in ground and satellite data by means of time domain impulse responses due to arbitrary external sources and in presence of a three-dimensional subsurface conductivity distribution. This approach is amenable to integrate with models that involve constantly augmented time series and require "on the fly" updates of geomagnetic models.

We have elaborated the underlying mathematical machinery for the case when basis functions used for spatial parameterization of magnetic field are given by SH functions. This choice was made owing to the ubiquity of SH basis in Earth's and planetary magnetism community. However, the approach is general and straightforward to extend to other basis functions should practical applications demand this.

We further showed that the effects from heterogeneities in subsurface electrical conductivity can dominate the radial magnetic field component and should be accounted for provided that some knowledge about three-dimensional subsurface conductivity structure for Earth is available. Contrary to the common presumption, the three-dimensional effects are significant during both quiet and disturbed magnetic conditions since the induction effect is transient, hence widely used selection criteria based on instant values of magnetic indices and local time cannot completely eliminate the effects of EM induction, making the modeling approach presented here a suitable tool that accounts for its transient nature.

Appendix A: Properties of Transfer Functions and Impulse Responses

Convolution integrals such as in Equations 20 and 28-29 represent a response of a medium to a time-varying extraneous current. These relations follow from the (often omitted) properties of a physical system that we model. We state these properties here and discuss implications. Our presentation closely follows a more detailed analysis by Svetov (1991).

1. **Linearity** allows us to define a response, $\zeta(t)$, of a medium at time t to an extraneous forcing as

$$\zeta(t) = \int_{-\infty}^{\infty} \mathcal{F}(t,t')\chi(t')dt', \tag{A1}$$

   where χ is the extraneous forcing that depends on time t' and $\mathcal{F}(t,t')$ is the medium Green's function that does not depend on the amplitude of the exerted force.
2. **Stationarity** implies that the response of a medium does not depend on the time of occurrence of the excitation. In this case $\mathcal{F}(t,t') \equiv f(t-t')$ and Equation A1 can be rewritten as a convolution integral

$$\zeta(t) = \int_{-\infty}^{\infty} f(t-\tau)\chi(\tau)d\tau = \int_{-\infty}^{\infty} f(\tau)\chi(t-\tau)d\tau, \tag{A2}$$

   where $f(t)$ represents the impulse response of a medium. In FD, the convolution integral reduces to

$$\tilde{\zeta}(\omega) = \tilde{f}(\omega)\tilde{\chi}(\omega), \tag{A3}$$

   where $\tilde{f}(\omega)$ is called the transfer function and we used tilde sign ($\tilde{\cdot}$) to denote complex quantities. Equation A2 and A3 are related through the Fourier transform

$$\tilde{f}(\omega) = \int_{-\infty}^{\infty} f(t)e^{i\omega t}\mathrm{d}t. \tag{A4}$$

3. Since we work in time domain with a real valued forcing, the impulse response is also **real.** To see implications of this, let us define the inverse Fourier transform of $\tilde{f}(\omega) = f_R(\omega) + \mathrm{i}f_I(\omega)$ as

$$\begin{aligned} f(t) &= \frac{1}{2\pi}\int_{-\infty}^{\infty}\tilde{f}(\omega)e^{-\mathrm{i}\omega t}\mathrm{d}\omega \\ &= \frac{1}{2\pi}\int_{-\infty}^{\infty}\Big[f_R(\omega)\cos(\omega t) + f_I(\omega)\sin(\omega t)\Big]\mathrm{d}\omega \\ &\quad + \frac{\mathrm{i}}{2\pi}\int_{-\infty}^{\infty}\Big[f_I(\omega)\cos(\omega t) - f_R(\omega)\sin(\omega t)\Big]\mathrm{d}\omega. \end{aligned} \tag{A5}$$

For an impulse response to be real, the last term in the integral A5 has to vanish. This is possible only if $f_R(\omega)$ and $f_I(\omega)$ are even and odd functions of the angular frequency ω, respectively. Therefore, Equation A5 reduces to

$$f(t) = \frac{1}{\pi}\int_{0}^{\infty}\Big[f_R(\omega)\cos(\omega t) + f_I(\omega)\sin(\omega t)\Big]\mathrm{d}\omega. \tag{A6}$$

4. Impulse response is **causal.** This property implies that $f(t) = 0$ for $t < 0$. Under this assumption, the convolution integral (A2) can be recast to

$$\zeta(t) = \int_{0}^{\infty} f(\tau)\chi(t-\tau)d\tau = \int_{-\infty}^{t} f(t-\tau)\chi(\tau)d\tau. \tag{A7}$$

Due to causality and taking into account Equation A6, the impulse response can be determined by using either only real or imaginary part of $\tilde{f}(\omega)$:

$$f(t) = \frac{2}{\pi}\int_{0}^{\infty} f_R(\omega)\cos(\omega t)\mathrm{d}\omega \tag{A8}$$

$$= -\frac{2}{\pi}\int_{0}^{\infty} f_I(\omega)\sin(\omega t)\mathrm{d}\omega. \tag{A9}$$

Note that for the sake of clarity, dependence on spatial variables and electrical conductivity pertinent to our application was omitted from the equations above.

In practice, we observed that using sine transform (A9) results in a slightly better accuracy compared to the cosine transform (A8) given the same filter length.

Appendix B: Digital Linear Filters

In order to carry out the sine transform (A9) efficiently, we applied the digital linear filter (DLF) method. DLF was introduced to geophysics by Ghosh in the early 1970s (Ghosh, 1971a, 1971b), as a means of fast computations for geoelectric resistivity responses. The method was subsequently improved and expanded to other methods by many authors, and a lot of filters have been published. There are two particular developments, out of all these improvements, which are relevant for our application: (1) The kernel under consideration was early on always Bessel functions of some sort, and it was Anderson (1973) who first applied it to Fourier sine and cosine transforms. (2) If the kernel computation is very expensive the lagged-convolution type DLF introduced by Anderson (1975) is very powerful, as additional times come at no or very little extra cost due to the reuse of the already computed kernels for new times. Although the use of DLF in geophysics is focused on Hankel and Fourier transforms in electromagnetics, the method itself works for any linear transform.

Werthmüller et al. (2019) presented a tool to design filters for any linear transform provided that there exist (a) an analytical transform pair or (b) a numerical computation in both domains with sufficient accuracy and precision over a wide range of argument values. We refer to that publication for an in-depth review of DLF in geophysics.

Using substitutions $t = e^x$ and $\omega = e^{-y}$ and multiplying by e^x we can rewrite (A9) as a convolution integral and approximate it by a N-point digital filter η as (Anderson, 1975)

$$f(t) \approx -\frac{2}{\pi}\sum_{n=1}^{N}\frac{f_I(b_n / t)\eta_n}{t}, \tag{B1}$$

where the log-spaced filter abscissa values b_n are a function of spacing Δ and shift ν,

$$b_n(\Delta,\nu) = \exp\Big[\Delta(-\lfloor (N+1)/2 \rfloor + n) + \nu\Big]. \tag{B2}$$

The optimal values for η_n, Δ and ν in Equations B1–B2 were found by following the method of Werthmüller et al. (2019). In this work, we designed a 50-point filter such that it requires as few values of $\tilde{f}(\omega)$ as possible without compromising accuracy. To this end, we used the following analytic transform pair

$$\frac{\pi \exp(-ab)}{2} = \int_0^\infty \frac{x}{a^2 + x^2}\sin(xb)dx. \tag{B3}$$

The Figure B1 shows the designed filter and its performance for the chosen analytic pair.

Note that the *naive* application of Equation B1 will require calculating $\tilde{f}(\omega)$ at $N \times N_t$ frequencies, where N_t is the length of an impulse response in time domain. This number can be drastically reduced by invoking the aforementioned lagged convolution approach. To give an example, for the one-year-long impulse response with the hourly time step (i.e., $N_t = 8{,}766$) our filter required evaluating a maximum of 112 frequencies that range ≈ 12 decades.

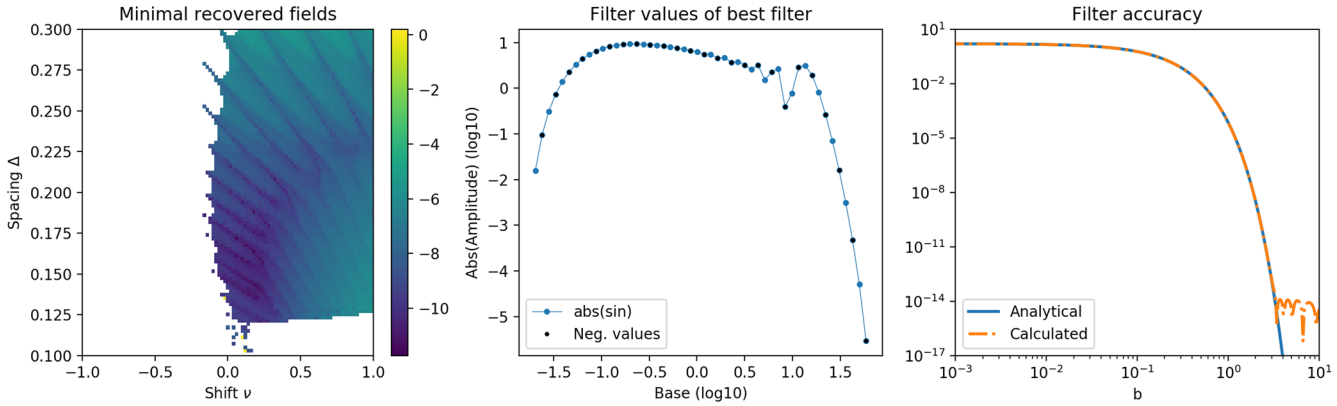

Figure B1. Left: minimum recovered value of the analytic pair (B3) as a function of spacing and shift. Center: filter values for the best filter with $\Delta = 0.114$ and $\nu = 1.07$. Right: the performance of the filter on the Equation B3.

Table B1
Filter used in this study to approximate the sine transform A9.

Base	Value
0.020351539057584585	0.015612515803531853
0.02394618633584547	−0.09462903411749914
0.028175748203049585	0.3117770493488479
0.0331523682171173	−0.7331733032969688
0.039007997604279074	1.3887195607048695
0.045897893843668	−2.256657066578928
0.05400473719916161	3.2805358935454616
0.06354347434512761	−4.3780014125702555

Table B1
Continued

Base	Value
0.0747670175110597	5.472633981207025
0.08797295025351011	−6.487680055307104
0.1035114176536700	7.379203081547922
0.121794410143077	−8.101406699379584
0.1433066871108987	8.655711019132568
0.16861862992378368	−9.017610106427929
0.19840136514614606	9.229490585407783
0.23344455894136176	−9.263211469329843
0.2746773544586444	9.201625018217383
0.3231930073442032	−8.981017420159862
0.38027787256818374	8.741193586707128
0.44744551113066483	−8.339636911178598
0.5264768209596123	8.017252694339163
0.6194672560404727	−7.484385258748044
0.728882385756068	7.168939484640828
0.8576232675496689	−6.5205283437188415
1.009103366216787	6.298382148011787
1.1873390592811512	−5.517835729490835
1.3970561281348315	5.467376261589812
1.6438150584726328	−4.53662000270438
1.9341584722647591	4.6731213626935695
2.2757846003123405	−3.691290054788441
2.6777513948763136	3.782371098562427
3.1507166942679676	−3.2281439933834775
3.7072208071793002	2.5592546437619657
4.36201900925792	−3.232119665813557
5.1324727678156865	1.5126346621525144
6.039010067691346	−2.2490157798136283
7.105667043450954	2.624917369559576
8.360725278884502	−0.38778344764051975
9.837461671301405	0.7697565678585556
11.575030742696057	−2.8607107883073972
13.619502791580832	3.1199881060456427
16.025085411278443	−1.9120353599090574
18.855560762285485	0.809753326019789
22.185976706870886	−0.2641923369068591
26.104636645033704	0.07088122130542221
30.715440810780017	−0.016121403161804555
36.14064110637662	0.0030871244528753875
42.524082516878885	−0.00047298225758749283
50.03501704852909	5.153158194873856e-05
58.87259131464845	−2.9723596837103312e-06

Data Availability Statement

Satellite and observatory input data used in this study as well as estimated time series of SH coefficients can be retrieved from https://doi.org/10.5281/zenodo.4047833. Subsurface conductivity model is available at https://doi.org/10.5281/zenodo.4058852.

Acknowledgments
This work was supported by the ESA through the Swarm DISC project. The staff of the geomagnetic observatories and INTERMAGNET are thanked for supplying high-quality observatory data, and BGS are thanked for making quality-controlled observatory hourly mean values openly available. We thank Chris Finlay, Nils Olsen, and Jakub Velímský for insightful discussions that facilitated this study.

References

Anderson, W. L. (1973). In: *Fortran IV programs for the determination of the transient tangential electric field and vertical magnetic field about a vertical magnetic dipole for an m-layer stratified earth by numerical integration and digital linear filtering* (Vol. *PB221240*, Technical Report). US Geological Survey.

Anderson, W. L. (1975). *Improved digital filters for evaluating fourier and hankel transform integrals* (Techical Report). US Geological Survey.

Arndt, D., Bangerth, W., Blais, B., Clevenger, T. C., Fehling, M., Grayver, A. V., et al. (2020). The deal.ii library, version 9.2. *Journal of Numerical Mathematics*, *28*, 131–146.000010151520200043. https://doi.org/10.1515/jnma-2020-0043. Retrieved from https://www.degruyter.com/view/journals/jnma/ahead-of-print/article-10.1515-jnma-2020-0043/article-10.1515-jnma-2020-0043.xml; https://doi.org/10.1515/jnma-2020-0043

Chulliat, A., Vigneron, P., & Hulot, G. (2016). First results from the Swarm dedicated ionospheric field inversion chain. *Earth Planets and Space*, *68*(1), 1–18.

Gauss, C. F. (1877). Allgemeine Theorie des Erdmagnetismus. *Werke*. Springer.

Ghosh, D. P. (1970). The application of linear filter theory to the direct interpretation of geoelectrical resistivity measurements. *Geophysical Prospecting*, *19*(2), 192–217. Retrieved from http://resolver.tudelft.nl/uuid:88a568bb-ebee-4d7b-92df-6639b42da2b2

Ghosh, D. P. (1971a). The application of linear filter theory to the direct interpretation of geoelectrical resistivity sounding measurements. *Geophysical Prospecting*, *19*(2), 192–217. https://doi.org/10.1111/j.1365-2478.1971.tb00593.x

Ghosh, D. P. (1971b). Inverse filter coefficients for the computation of apparent resistivity standard curves for a horizontally stratified earth. *Geophysical Prospecting*, *19*(4), 769–775. https://doi.org/10.1111/j.1365-2478.1971.tb00915.x

Grayver, A. V., & Kolev, T. V. (2015). Large-scale 3D geoelectromagnetic modeling using parallel adaptive high-order finite element method. *Geophysics*, *80*(6), E277–E291.

Grayver, A. V., Munch, F. D., Kuvshinov, A. V., Khan, A., Sabaka, T. J., & Tøffner-Clausen, L. (2017). Joint inversion of satellite-detected tidal and magnetospheric signals constrains electrical conductivity and water content of the upper mantle and transition zone. *Geophysical Research Letters*, *44*(12), 6074–6081. https://doi.org/10.1002/2017GL073446

Grayver, A. V., van Driel, M., & Kuvshinov, A. V. (2019). Three-dimensional magnetotelluric modeling in spherical earth. *Geophysical Journal International*, *217*(1), 532–557.

Guzavina, M., Grayver, A., & Kuvshinov, A. (2019). Probing upper mantle electrical conductivity with daily magnetic variations using global-to-local transfer functions. *Geophysical Journal International*, *219*(3), 2125–2147.

Honkonen, I., Kuvshinov, A., Rastätter, L., & Pulkkinen, A. (2018). Predicting global ground geoelectric field with coupled geospace and three-dimensional geomagnetic induction models. *Space Weather*, *16*(8), 1028–1041. https://doi.org/10.1029/2018SW001859

Kelbert, A. (2020). The role of global/regional earth conductivity models in natural geomagnetic hazard mitigation. *Surveys in Geophysics*, *41*(1), 115–166.

Koch, S., & Kuvshinov, A. (2013). Global 3-D EM inversion of Sq variations based on simultaneous source and conductivity determination: Concept validation and resolution studies. *Geophysical Journal International*, *195*(1), 98–116.

Kuvshinov, A. (2008). 3-D global induction in the oceans and solid Earth: Recent progress in modeling magnetic and electric fields from sources of magnetospheric, ionospheric and oceanic origin. *Surveys in Geophysics*, *29*, 139–186. https://doi.org/10.1007/s10712-008-9045-z

Kuvshinov, A., Avdeev, D., & Pankratov, O. (1999). Global induction by sq and dst sources in the presence of oceans: Bimodal solutions for non-uniform spherical surface shells above radially symmetric earth models in comparison to observations. *Geophysical Journal International*, *137*(3), 630–650.

Macmillan, S., & Olsen, N. (2013). Observatory data and the swarm mission. *Earth Planets and Space*, *65*(11), 15.

Maus, S., & Weidelt, P. (2004). Separating the magnetospheric disturbance magnetic field into external and transient internal contributions using a 1D conductivity model of the earth. *Geophysical Research Letters*, *31*(12), L12614. https://doi.org/10.1029/2004GL020232

Munch, F. D., Grayver, A. V., Guzavina, M., Kuvshinov, A. V., & Khan, A. (2020). Joint inversion of daily and long-period geomagnetic transfer functions reveals lateral variations in mantle water content. *Geophysical Research Letters*, *47*(10), e2020GL087222. https://doi.org/10.1029/2020GL087222

Olsen, N. (1997). Ionospheric f region currents at middle and low latitudes estimated from magsat data. *Journal of Geophysical Research*, *102*(A3), 4563–4576.

Olsen, N. (1999). Induction studies with satellite data. *Surveys in Geophysics*, *20*(3–4), 309–340.

Olsen, N., Glassmeier, K.-H., & Jia, X. (2010). Separation of the magnetic field into external and internal parts. *Space Science Reviews*, *152*(1–4), 135–157.

Olsen, N., & Kuvshinov, A. (2004). Modeling the ocean effect of geomagnetic storms. *Earth Planets and Space*, *56*(5), 525–530.

Olsen, N., Sabaka, T. J., & Lowes, F. (2005). New parameterization of external and induced fields in geomagnetic field modeling, and a candidate model for IGRF 2005. *Earth Planets and Space*, *57*(12), 1141–1149.

Price, A. (1967). Electromagnetic induction within the Earth. In: *International geophysics* (Vol. 11, pp. 235–298). Elsevier.

Püthe, C., & Kuvshinov, A. (2014). Mapping 3-d mantle electrical conductivity from space: A new 3-d inversion scheme based on analysis of matrix q-responses. *Geophysical Journal International*, *197*, 768–784. https://doi.org/10.1093/gji/ggu027

Püthe, C., Manoj, C., & Kuvshinov, A. (2014). Reproducing electric field observations during magnetic storms by means of rigorous 3-d modeling and distortion matrix co-estimation. *Earth Planets and Space*, *66*(1), 162.

Sabaka, T. J., Olsen, N., & Purucker, M. E. (2004). Extending comprehensive models of the Earth's magnetic field with ørsted and CHAMP data. *Geophysical Journal International*, *159*(2), 521–547.

Sabaka, T. J., Olsen, N., Tyler, R. H., & Kuvshinov, A. (2015). CM5, a pre-Swarm comprehensive geomagnetic field model derived from over 12 yr of CHAMP, ørsted, SAC-C and observatory data. *Geophysical Journal International*, *200*(3), 1596–1626.

Sabaka, T. J., Tøffner-Clausen, L., Olsen, N., & Finlay, C. C. (2018). A comprehensive model of Earth's magnetic field determined from 4 years of Swarm satellite observations. *Earth Planets and Space*, *70*(1), 130.

Schmucker, U. (1985). *Magnetic and electric fields due to electromagnetic induction by external sources, electrical properties of the Earth's interior*. New–Series: Landolt-Bornstein.

Schmucker, U. (1999). A spherical harmonic analysis of solar daily variations in the years 1964–1965: Response estimates and source fields for global induction–ii. results. *Geophysical Journal International*, *136*(2), 455–476.

Schuster, A. (1889). The diurnal variation of terrestrial magnetism. *Philosophical Transactions of the Royal Society of London*, *180*, 467–518.

Sun, J., & Egbert, G. D. (2012). Spherical decomposition of electromagnetic fields generated by quasi-static currents. *GEM-International Journal on Geomathematics*, *3*(2), 279–295.

Sun, J., Kelbert, A., & Egbert, G. D. (2015). Ionospheric current source modeling and global geomagnetic induction using ground geomagnetic observatory data. *Journal of Geophysical Research: Solid Earth*, *120*(10), 6771–6796. https://doi.org/10.1002/2015JB012063

Svetov, B. S. (1991). Transfer functions of the electromagnetic field (in russian). *Fizika Zemli*, 1, 119–128.

Thomson, A. W., & Lesur, V. (2007). An improved geomagnetic data selection algorithm for global geomagnetic field modeling. *Geophysical Journal International*, *169*(3), 951–963.

Velímský, J., Everett, M. E., & Martinec, Z. (2003). The transient Dst electromagnetic induction signal at satellite altitudes for a realistic 3-D electrical conductivity in the crust and mantle. *Geophysical Research Letters*, *30*(7), 1355. https://doi.org/10.1029/2002GL016671

Velímský, J., & Martinec, Z. (2005). Time-domain, spherical harmonic-finite element approach to transient three-dimensional geomagnetic induction in a spherical heterogeneous Earth. *Geophysical Journal International*, *161*(1), 81–101.

Werthmüller, D., Key, K., & Slob, E. C. (2019). A tool for designing digital filters for the Hankel and Fourier transforms in potential, diffusive, and wavefield modeling. *Geophysics*, *84*(2), F47–F56.

Yamazaki, Y., & Maute, A. (2017). Sq and EEJ–A review on the daily variation of the geomagnetic field caused by ionospheric dynamo currents. *Space Science Reviews*, *206*(1–4), 299–405. https://doi.org/10.1190/geo2018-0069.1